An Investigation of the Dynamics of the East Greenland Current in Fram Strait Based on a Simple Analytical Model

PAWEL SCHLICHTHOLZ*

Institute of Oceanology, Polish Academy of Sciences, Sopot, Poland

MARIE-NOËLLE HOUSSAIS

Laboratoire d'Océanographie Dynamique et de Climatologie, UMR CNRS/ORSTOM/Université Pierre et Marie Curie, Paris, France

(Manuscript received 28 April 1997, in final form 14 October 1998)

ABSTRACT

The East Greenland Current (EGC) in Fram Strait is examined in summer, based on the hydrographic data from the MIZEX 84 experiment, and its dynamics is further analyzed using a simple analytical model. From the observed density field, the southward geostrophic transport relative to the bottom in the EGC is estimated to be about 4 Sv (Sv $\equiv 10^6$ m^3 s^{-1}) at 78.4°N, which, assuming a ratio 1:1 between the bottom and the relative transports as suggested in the literature, allows one to postulate a 4 Sv bottom transport. The hydrographic data also reveal a northward gradient of potential energy along the East Greenland slope, between 77.5°N and 80.5°N. Such a gradient is the prerequisite for the existence of the joint effect of baroclinicity and relief (JEBAR), which is here proposed as a driving mechanism for the bottom transport in the EGC.

A model with idealized topography and a density distribution prescribed from the above data is constructed based on a steady-state vorticity equation in which the JEBAR forcing is balanced by damping due to friction. According to the model, the JEBAR-induced flow consistent with such a gradient is southward. Validity requirements on the model assumptions constrain the range of allowable values for the model friction parameters. The prediction of a 4 Sv bottom transport can be obtained for a total amount of friction within this range.

Both internal and bottom friction are considered in the model. The relative importance of these two types of friction determines to what extent the JEBAR controls the bottom or the depth-averaged flow and constrains the local characteristics of the flow. If only internal friction is allowed in the model, the required value of the friction coefficient is consistent with the values reported in the literature while, if bottom friction alone is allowed, prediction of a 4 Sv bottom transport is possible only for a relatively high friction coefficient. In terms of flow structure, the best agreement between the predicted flow and the current meter data reported in the literature is obtained for a regime with both types of friction in which, however, internal friction predominates.

1. Introduction

The East Greenland Current (EGC) is a major component of the current system of the Nordic (Greenland–Norwegian–Iceland) seas and an important dynamical link between the Arctic Ocean and the North Atlantic Ocean. In the upper layer, the EGC carries southward, across the Nordic seas, the polar water (PW), which has been formed in the Arctic Ocean. The relatively high surface current velocities contribute efficiently, together with the wind stress, to driving the sea ice out of the Arctic Ocean through Fram Strait (Moritz and Colony 1988). As a whole, the total ice and surface water outflow achieved by the current constitutes the main freshwater sink for the Arctic Ocean. In addition, by being responsible for a heat deficit export of approximately 30×10^{12}–40×10^{12} W out of the Arctic Ocean, the sea ice outflow constitutes the major heat source for the Arctic Ocean (e.g., Rudels 1987). The EGC also contributes to advecting anomalies of the Arctic Ocean water mass characteristics, which may ultimately affect the sea ice distribution and the stratification in the Nordic seas.

In the intermediate depth range, the EGC returns to the south the relatively warm and salty Atlantic water (AW), which has been carried northward by the West Spitsbergen Current (WSC) and subsequently sinks below the PW in Fram Strait. The return flow of AW is made partly of water that has recirculated around the Arctic Ocean and partly of water that has turned back

* Current affiliation: Laboratoire d'Océanographie Dynamique et de Climatologie, Paris, France.

Corresponding author address: Dr. Marie-Noëlle Houssais, LODYC, University de Paris VI, 4 Place Jussieu, Tour 14, 2eme Etage, 75232 Paris Cedex 05 France.

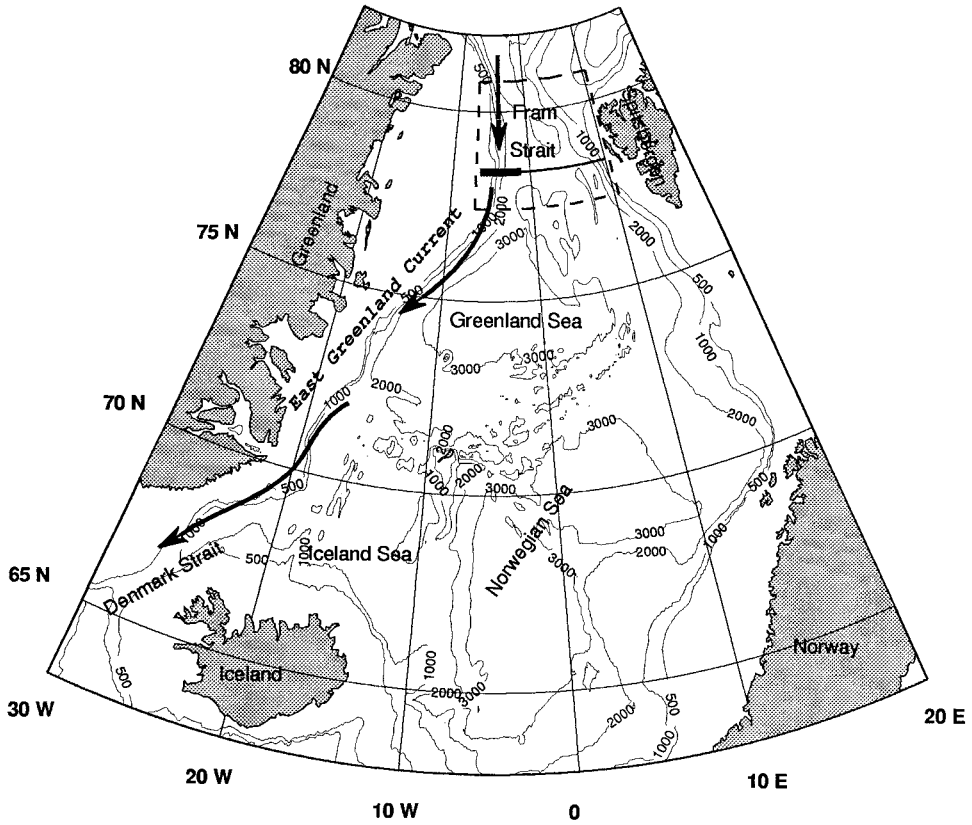

FIG. 1. Bathymetric chart of the Nordic seas showing the extent of the domain under investigation. The meridional extent of the box corresponds to the scale used to estimate the alongslope gradient of potential energy (PE) from available observations. The zonal extent at 78.4°N is taken from the section of observations displayed in Fig. 2. Superimposed as a bold line is the corresponding model cross section (see Fig. 4). Also shown is a schematic representation of the surface circulation in the East Greenland Current.

in Fram Strait without contributing to the inflow to the north (Aagaard et al. 1985). The strength of this return flow is determinative for the global heat and salt budgets of the Arctic Ocean. Farther to the south the intermediate layer of the EGC is additionally fed by admixtures of colder and fresher convection products from the interior of the Greenland Sea (GS). Ultimately, the EGC contributes a significant part to the Denmark Strait overflow water (Strass et al. 1993), which initiates the deep branch of the so-called ''conveyor belt'' circulation of the World Ocean (Broecker 1991).

The EGC follows the eastern continental margin of Greenland (Fig. 1). The main body of the flow lies over the slope with maximum geostrophic velocities referred to 200 m of the order of 20–30 cm s^{-1} at the surface (Aagaard and Coachman 1968). Still, geostrophic velocities referred to 500 m as high as 96 cm s^{-1} have been reported near the ice edge (Paquette et al. 1985). Although the current exhibits strong vertical shears, significant velocities of the order of a few centimeters per second are measured near the bottom at 79°N in the upstream region of the current (Foldvik et al. 1988). The bottom flow there is characterized by a significant offshore component as well as an upslope increase of the alongslope component. Cross-slope variations of the alongslope flow have also been observed at the surface farther to the south, at 75°N, where the current exhibits cores of maximum velocity above the East Greenland slope (Fahrbach et al. 1995).

The present study focuses on the EGC dynamics, volume transport, and flow structure in Fram Strait between 77° and 81°N (Fig. 1). This region has been selected because of the relatively large amount of quasi-synoptic hydrographic data available in the EGC at these latitudes, as a result of the Marginal Ice Zone Experiment 1984 (MIZEX 84). Direct current measurements in the EGC at 79°N indicate a transport of 3 Sv (Sv $\equiv 10^6$ m^3 s^{-1}) in the upper 700 m of the water column (Foldvik et al. 1988). Indirect estimates based on considerations on the exchange through the strait or on requirements on the Arctic Ocean mass balance spread between 2 Sv (Mosby 1962) and 7.1 Sv (Aagaard and Greisman 1975), while Rudels (1987) proposes a transport of 4.1 Sv. Estimates based on geostrophic velocities referred to some reference level give smaller values. For instance, a transport of 2 Sv referred to 500 m is reported by Paquette et al. (1985) at 78°N in fall 1981 while, as will be shown in section 2 of this paper, the summer hydro-

graphic data from the MIZEX 84 experiment provide an estimate of the transport relative to the bottom of approximately 4 Sv at 78.4°N.

Considering possible forcings, the wind stress curl in summer in Fram Strait is very weak (Jònsson 1991), which contrasts with the GS where the wind should be able to drive a strong annual mean circulation (e.g., Aagaard 1970). The surface flow of the EGC is usually considered to be the outflowing part of an estuarine circulation driven by density differences between the lighter surface waters of the Arctic Ocean and the denser Atlantic waters of the GS (Stigebrandt 1981). The width of the strait is large enough for rotational effects to maintain a narrow boundary flow along the western rim of the strait, associated with a sloping front between the in- and outflowing water masses. Such buoyancy-driven exchanges have been studied by means of laboratory experiments in a rotating tank (Wadhams et al. 1979) or using ''lock exchange'' experiments (Hunkins and Whitehead 1992). They have also been investigated through modeling based on the density distribution observed in the strait (Manley et al. 1987). All these experiments provide estimates for the PW volume transport in the EGC. Manley et al. (1987) found a transport of 1.1 Sv while applying relation (39) of Hunkins and Whitehead (1992) gives a smaller transport (0.35 Sv).

The origin of a deep flow in the EGC has been much less documented. Still, at 79°N the bottom component of the transport is believed to contribute half of the total transport of the current (Foldvik et al. 1988). A barotropic circulation in Fram Strait has previously been suggested by Greisman (1976) in the form of a topography-steered cyclonic gyre joining part of the flow of the WSC to the EGC, or by Stigebrandt (1981) as a result of tidal pumping. Considering the likely important role of the East Greenland slope in the EGC dynamics, the present study proposes to investigate another mechanism, the JEBAR (joint effect of baroclinicity and relief), as a possible forcing for a depth-independent component of the EGC. The existence of the JEBAR forcing is subject to the presence of an along-isobath gradient of potential energy (PE), which is indeed observed in the EGC (see section 4). The JEBAR has been previously shown to be responsible for driving slope currents such as the Leeuwin Current in the Indian Ocean (Huthnance 1984). It has also been shown to be an important component of the vorticity balance of the Gulf Stream (Salmon 1994; Salmon and Ford 1995; Myers et al. 1996). That the JEBAR may be relevant in the Nordic seas has already been stipulated by Slordal and Weber (1996), who studied the transient response to the JEBAR forcing of a frictionless flow in a channel bounded by a shelf-slope region on both sides.

In this context, we designed a steady-state model based on simplified depth-averaged vorticity dynamics, that is, where the JEBAR appears as the main forcing and is to the first order balanced by friction. Equations are solved analytically after both the model geometry and density structure are idealized according to typical Fram Strait conditions. The model is used to derive the bottom component of the geostrophic flow and to estimate a range of possible bottom transport values consistent with the model assumptions. By contrast with previous similar applications, which only included either the bottom (e.g., Huthnance 1984) or the internal (e.g., Salmon 1994) friction, the combined effects of the two types of friction are considered in the model, which allows us to investigate their respective impact on the flow structure.

In our model, as by nature, the JEBAR is entirely determined by the density distribution relative to the bottom topography. The information contained in the density field is additionally used in the model to specify the geostrophic flow relative to the bottom. In order to obtain an accurate description of the density field relative to the topography, the hydrographic data from the MIZEX 84 experiment and the bottom topography data have been interpolated on the same horizontal grid using a variational interpolation scheme (Schlichtholz and Houssais 1995). The interpolated hydrographic fields can be regarded as the large-scale time-mean summer distributions in 1984. It should be noted that our model is simpler than Huthnance's (1984) model since, by specifying the density distribution, it neglects how such a distribution is modified by the induced flow.

The present analysis is organized as follows. First, in section 2, the available hydrographic data from the MIZEX 84 experiment at 78.4°N in the EGC are presented and the distribution of the associated geostrophic flow relative to the bottom is discussed. An estimate of the corresponding relative transport is proposed as a typical summer value for the EGC in Fram Strait. In addition, based on current meter information from the literature, the bottom flow in the EGC is discussed and a bottom transport value postulated. In section 3 the analytical model is described, while in section 4 the model is calibrated by adjusting the model parameters to the specific geometry and dynamics of the EGC in Fram Strait. Model results are presented in section 5 in terms of alongslope transports as well as flow structure. In section 6, a discussion of the model validity is presented based on a posteriori verification of the model dynamical assumptions and a comparison of the model results with relevant information from other studies. A summary is given in section 7.

2. The EGC at 78.4°N

Much of the EGC flow structure can be understood from the hydrographic conditions at 78.4°N. The dominant hydrographic feature in the area is the East Greenland Polar Front (EGPF), which separates the cold, fresh, and light PW west of the front from the warmer, more saline and denser AW to the east. The position of the EGPF is usually considered to coincide with the upper isotherm $\theta = 0$°C (e.g., Paquette et al. 1985). At

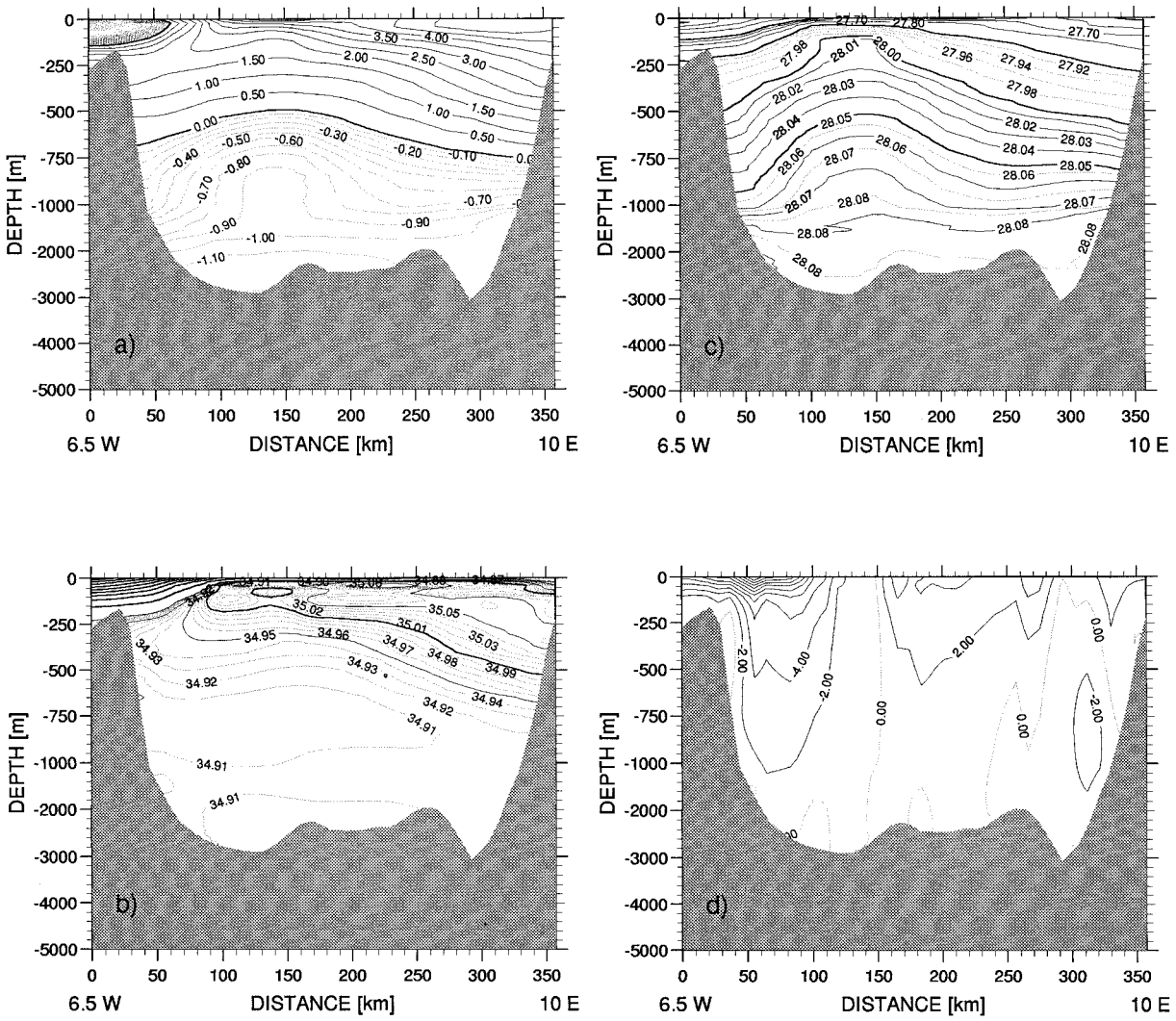

FIG. 2. Vertical distributions of (a) potential temperature (in °C), (b) salinity (in psu), (c) density referred to the surface (in sigma units), and (d) meridional geostrophic velocity component referred to the bottom (in 10^{-2} m s^{-1}) along the section at 78.4°N shown in Fig. 1. Positive values indicate northward velocities. Distributions are deduced from the MIZEX 84 observations.

78.4°N, the 0°C isotherm defines a wedge of PW flowing over the East Greenland shelf and slope (Fig. 2a). The isotherm outcrops at the surface approximately 30 km off the shelf break at a location where the ocean depth is about 2200 m. The EGPF is even more marked in salinity (Fig. 2b), resulting in a clear signature in the density distribution as well (Fig. 2c). The resulting baroclinicity of the current, as illustrated by the vertical distribution of the geostrophic velocity relative to the bottom (Fig. 2d), is particularly obvious over the slope. Even though the distribution has been smoothed by the interpolation scheme, the maximum relative velocity is still larger than 20 cm s^{-1}. The core of maximum velocity is located in the surface layer and is encountered over depths between 1500 and 2000 m, in agreement with Foldvik et al.'s (1988) current measurements at 79°N, who found the largest upper-layer velocities at the middle of their three mooring section, over the isobath 1700 m. Despite considerable vertical shears, the relative velocities are still important in the intermediate (AW) or deep (DW) water range. At 700 m, that is, the depth where the lower $\theta = 0$°C isotherm intersects the East Greenland slope at 78.4°N, the maximum relative velocity is about 3 cm s^{-1}.

From the velocity distribution at 78.4°N, the southward volume transport relative to the bottom at this latitude can be estimated. The volume transport has been cumulated eastward from 6.5°W assuming that, west of this longitude, the flow is likely to be involved in the well-known semipermanent clockwise gyre sitting on the East Greenland shelf (e.g., Budeus and Schneider 1995), without contributing significantly to the south-

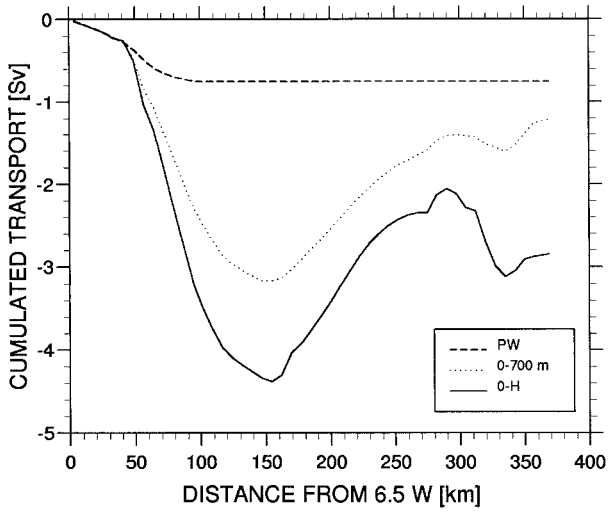

FIG. 3. Cross-slope distribution of the meridional geostrophic volume transport (in 10^6 m^3 s^{-1}) at 78.4°N, based on the velocity distribution in Fig. 2d for the total water column (solid line), the upper 700 m, (dotted line), and the polar water (PW) layer (dashed line). The transport is cumulated from 6.5°W eastward.

ward transport. If the outer limit of the EGC is taken to be the location of the maximum cumulated transport, then the total relative transport in the EGC would be a little more than 4 Sv (Fig. 3). This estimate is subject to a methodology error of about 0.5 Sv and therefore depends only slightly on the configuration of the interpolation method used to reconstruct the density distribution. Probably more important is the uncertainty on our estimate due to the time variability of the flow. For instance, the discrepancy between our relative transport and the Foldvik et al. (1988) estimate at 79°N for approximately the same period can be attributed to the different sampling timescales (seasonal in our case, yearly averaged in Foldvik et al.'s). From Fig. 3, a transport of 3.2 Sv is found in the upper 700 m of the water column, which should be compared with the 3 Sv found by Foldvik et al. (1988), of which only a half was postulated to be achieved by the relative component of the flow. On the other hand, taking the upper and lower 0°C isotherms as the boundaries between the PW and the AW and between the AW and the DW, respectively, one obtains from Fig. 3 volume transports for the PW, the AW, and the DW that are 0.8 Sv, 2.4 Sv, and 1.2 Sv, respectively. Our PW volume transport is therefore smaller than transports proposed by other authors, namely the 1.1 Sv obtained by Manley et al. (1987), the 1.8 Sv proposed by Aagaard and Greisman (1975), or the 0.9 Sv obtained by Rudels (1987), probably as a result of neglecting in our case the contribution of the bottom flow. Still, despite the above uncertainty on the relative-to-bottom transport of the EGC in Fram Strait, a value of 4 Sv will be assumed in the following analysis as a reasonable estimate of this transport in summer.

An estimate of the bottom component in the southward flow of the EGC in Fram Strait can be obtained using current measurements carried out during the MIZEX 84 experiment at 78.4°N at a mooring located over the 1000-m isobath (Manley et al. 1987). The vertical shear between the meridional velocities recorded at 120 m and 420 m is comparable with the one calculated from our density field at approximately the same latitude (Fig. 2). Subtracting the relative velocities in Fig. 2d from the current meter velocities at the same level, the same value of about 7 cm s^{-1} is obtained at the two levels and can be regarded as an estimate of the bottom component of the flow. This bottom component may vary across the slope (Foldvik et al. 1988) but it can be expected to be of the order of 5–10 cm s^{-1}. If, following these authors, a ratio of 1:1 is assumed between the bottom and the relative-to-bottom transport of the EGC, the total transport in the upper and intermediate layers of the EGC through the section considered in Fig. 3 would be approximately 6.5 Sv. Such a value is very close to the estimate obtained by Aagaard and Greisman (1975), who, assuming a zero net transport through Fram Strait and neglecting the transport in the DW range, obtained individual transports of 7.1 Sv in opposite directions for the EGC and for the WSC. Given the same ratio, the bottom transport in the EGC through our selected section would be 4 Sv and the total transport would be about 8 Sv.

3. The analytical model

The derivation of the model equations is first summarized before the basic simplifications that apply to the present case study are presented. The general dynamical framework of the model follows that of other studies (e.g., Huthnance 1984; Mertz and Wright 1992).

a. Governing equations

Consider a frictional flow satisfying the hydrostatic and Boussinesq approximations. Assuming that the advection of horizontal momentum can be neglected and that internal dissipation can be parameterized by Rayleigh friction (Salmon 1990), the steady-state momentum equation governing the horizontal velocity, $\mathbf{u} = (u, v)$, is

$$\mathbf{z} \times f\mathbf{u} = -\frac{1}{\rho_0}\nabla p - \Lambda\mathbf{u} + \delta_E \frac{1}{\rho_0}\tau_z. \qquad (1)$$

In (1), z is the vertical coordinate and $\mathbf{z}$ the corresponding upward unit vector, ∇ is the horizontal gradient operator, f is the Coriolis parameter, p is the pressure, ρ_0 is a reference density, Λ is the eddy decay coefficient (assumed constant), τ is a horizontal stress resulting from wind action at the sea surface or from friction on the bottom, and δ_E is equal to 1 in the surface and bottom Ekman layers and 0 elsewhere. A space coordinate, when used as a subscript, denotes differentiation with respect to this coordinate.

The hydrostatic equation is

$$p_z = -\rho g, \tag{2}$$

where ρ is the seawater density and g is the earth gravity.

The continuity equation can be written as

$$\nabla \cdot \mathbf{u} + w_z = 0, \tag{3}$$

where w is the vertical component of the velocity.

The boundary conditions are given by the rigid-lid approximation at the sea surface,

$$w = 0 \quad \text{at } z = 0, \tag{4}$$

and the constraint of no-normal flow through the bottom,

$$w = -\mathbf{u} \cdot \nabla H \quad \text{at } z = -H, \tag{5}$$

where H is the ocean depth.

Using (2) to express p as a function of the bottom pressure Φ and of the density distribution, (1) can be rewritten as

$$\mathbf{u} = -\frac{1}{f\rho_0}\left\{\left[\nabla\Phi - g\nabla\left(\int_{-H}^{z} \rho\, dz'\right)\right](\times \mathbf{z} + \epsilon) + \delta_E(\epsilon + \mathbf{z}\times)\,\tau_z\right\}, \tag{6}$$

where $\epsilon = \Lambda/f$ has been assumed to be such that

$$\epsilon^2 \ll 1. \tag{7}$$

Vertical integration of (6) provides a relationship between the new unknown Φ and the nondivergent streamfunction of the depth-integrated flow, Ψ:

$$\mathbf{z}\times\nabla\Psi = -\frac{1}{f\rho_0}\{[H\nabla\Phi + \nabla(\rho_0\chi)]\,(\times \mathbf{z} + \varepsilon) + (\epsilon + \mathbf{z}\times)\,(\tau_s - \tau_b)\}, \tag{8}$$

where Ψ is defined as

$$\mathbf{z}\times\nabla\Psi = \int_{-H}^{0} \mathbf{u}\, dz. \tag{9}$$

In (8), $\rho_0\chi$ is the total potential energy of a water column of unit area,

$$\rho_0\chi = g\int_{-H}^{0} z\rho\, dz, \tag{10}$$

and τ_s and τ_b are the surface and bottom stress, respectively. Dividing (8) by H and reintroducing the bottom pressure term into (6) provides the following expression for the horizontal flow velocity:

$$\mathbf{u} = \frac{\mathbf{z}\times\nabla\Psi}{H} + (1 + \epsilon\mathbf{z}\times)\,\mathbf{u}_r' + (\epsilon + \mathbf{z}\times)\frac{\tau_s - \tau_b}{f\rho_0 H} + \delta_E(1 - \epsilon\mathbf{z}\times)\,\mathbf{u}_E, \tag{11}$$

where $\mathbf{u}_E = (u_E, v_E)$ is the Ekman velocity defined as

$$\mathbf{u}_E = \frac{\tau_z\times\mathbf{z}}{f\rho_0} \tag{12}$$

and $\mathbf{u}_r' = (u_r', v_r')$ is defined as

$$\mathbf{u}_r' = \left[\frac{g}{f\rho_0}\nabla\left(\int_{-H}^{z}\rho\, dz'\right) + \frac{\nabla\chi}{fH}\right]\times\mathbf{z}. \tag{13}$$

In (13), one can show that $\mathbf{u}_r' = \mathbf{u}_r - \overline{\mathbf{u}}_r$ is the geostrophic shear velocity since $\mathbf{u}_r = (u_r, v_r)$, the geostrophic velocity relative to the bottom, can be expressed as

$$\mathbf{u}_r = \frac{g}{f\rho_0}\int_{-H}^{z}(\nabla\rho\times\mathbf{z})\, dz' \tag{14}$$

and $\overline{\mathbf{u}}_r = (\overline{u}_r, \overline{v}_r)$, its vertical average, is given by

$$\overline{\mathbf{u}}_r = \mathbf{z}\times\left(\frac{\nabla\chi}{fH} + \frac{g}{f}\frac{\rho_b}{\rho_0}\nabla H\right), \tag{15}$$

where ρ_b is the density at the bottom.

In (11), the bottom stress τ_b is parameterized by a linear function of the velocity just above the bottom Ekman layer, $\mathbf{u}_b = (u_b, v_b)$; that is,

$$\tau_b = \rho_0 r\mathbf{u}_b, \tag{16}$$

where r, the resistance coefficient with dimension of a velocity, is assumed constant. Assuming that the horizontal pressure gradient is uniform across the bottom Ekman layer, (11) can be used at $z = -H$ to obtain an estimate of $\mathbf{u}_b$:

$$\mathbf{u}_b = (1 - \mu\mathbf{z}\times)\times\left[\frac{\mathbf{z}\times\nabla\Psi}{H} - (1 + \epsilon\mathbf{z}\times)\,\overline{\mathbf{u}}_r + (\epsilon + \mathbf{z}\times)\frac{\tau_s}{f\rho_0 H}\right], \tag{17}$$

where $\mu = r/fH$ is such that

$$\mu^2 \ll 1. \tag{18}$$

Reintroducing (16) and (17) into (11) yields the following expression for the horizontal flow velocity:

$$\mathbf{u} = (\mu + \mathbf{z}\times)\frac{\nabla\Psi}{H} + \mu\mathbf{z}\times\overline{\mathbf{u}}_r + (1 + \epsilon\mathbf{z}\times)\,\mathbf{u}_r' + (\epsilon + \mu + \mathbf{z}\times)\frac{\tau_s}{f\rho_0 H} + \delta_E(1 - \epsilon\mathbf{z}\times)\,\mathbf{u}_E. \tag{19}$$

Outside the Ekman layers, the horizontal velocity therefore depends on the density distribution and on the wind stress, which can both be known from observations, and on Ψ. In order to estimate Ψ, a vorticity tendency equation is first formed by taking the curl of the depth-average of the horizontal momentum equation (1):

$$J\left(\Psi, \frac{f}{H}\right) = J(\chi, H^{-1}) - \nabla \cdot \left(\epsilon \frac{f}{H} \nabla \Psi\right) + \mathbf{z} \cdot \nabla \times \left(\frac{\tau_s - \tau_b}{\rho_0 H}\right), \quad (20)$$

where $J(A, B) = A_x B_y - A_y B_x$ is the Jacobian operator. The term $J(\chi, H^{-1})$ represents the JEBAR, a forcing on the depth-averaged flow which will be shown of primary importance in the context of the EGC in Fram Strait. The JEBAR term is a correction to the topographic vortex stretching term on the left-hand side of (20) to take into account the fact that the latter involves the depth-averaged velocity instead of the bottom velocity. A more detailed discussion of this term can be found, for example, in Huthnance (1984) or Mertz and Wright (1992) and more recently in Myers et al. (1996) or Sakamoto and Yamagata (1996).

Introducing (16) and (17) into (20) and neglecting small terms provides the following relation between Ψ and the observed flow variables:

$$J\left(\Psi, \frac{f}{H}\right) = J(\chi, H^{-1}) - \nabla \cdot \left(\epsilon \frac{f}{H} \nabla \Psi\right) + \mathbf{z} \cdot \nabla \times \left[\mu f \left(\frac{\nabla \Psi \times \mathbf{z}}{H} + \overline{\mathbf{u}}_r\right) + (1 - \mu \mathbf{z} \times) \frac{\tau_s}{\rho_0 H}\right]. \quad (21)$$

Relations (21) and (19) combined with (10), (13), and (15) form the basic set of equations to calculate the barotropic and total velocities, respectively. Assuming that the environmental parameters f and H are known, the model input consists of the density ρ (from which $\mathbf{u}'_r$, $\overline{\mathbf{u}}_r$, and χ are estimated), the wind stress τ_s, and the friction coefficients r and Λ.

b. Basic simplifications

We are interested in a flow over a steep continental slope (the East Greenland slope). To have such a problem analytically tractable, several idealizations concerning the domain geometry, the density distribution, and the dynamics should be imposed. These assumptions are listed below and will be a posteriori validated in section 6a.

The bottom topography is approximated by a uniformly sloping plane of width L_c. Assuming that x and y are the cross- and alongslope coordinates respectively, the bottom depth is independent of y. Taking the origin of the x coordinate at the coast, the bottom depth can be defined as

$$H = \frac{H_b}{L_c} x, \qquad 0 \le x \le L_c, \quad (22)$$

where H_b is the depth at the slope base.

The alongslope length scale of the flow is assumed to be much larger than the cross-slope scale so that the flow is independent of the alongslope coordinate, which leads to

$$\int_{-H}^{0} v_y \, dz = \Psi_{xy} = 0, \quad (23)$$

which, using the condition of zero transport normal to the coast, is changed into

$$\Psi_y = 0. \quad (24)$$

In the ocean interior far from the continental slope one expects frictional forces to be much smaller than the Coriolis force, that is, the flow to be close to geostrophic equilibrium. This assumption is equivalent to condition (7) on the internal friction. In the slope region, the flow is assumed to be primarily directed along the isobaths, which implies that internal friction there can only be neglected in the balance of the alongslope flow or, equivalently, that

$$R_\epsilon = \epsilon \frac{U_0}{V_0} \ll 1, \quad (25)$$

where U_0 and V_0 are characteristic values for the cross-slope and alongslope components of the velocity, respectively. If one also requires that bottom friction associated with this flow component be negligible, then a condition similar to (25) is obtained by considering the balance of the depth-integrated flow; that is,

$$R_\mu = \frac{r}{f} \frac{U_{b0}}{(\Psi_x)_0} \ll 1, \quad (26)$$

where U_{b0} and $(\Psi_x)_0$ are characteristic values for the cross-slope bottom velocity and for the depth-integrated alongslope flow, respectively. Condition (26) is equivalent to neglecting the alongslope component of the bottom Ekman transport when compared with the total alongslope transport.

Additional assumptions can be made based on our knowledge of the dynamics of the EGC in Fram Strait. First, the wind stress is assumed to be small (see section 6a) so that all terms involving τ_s are neglected in the model. This assumption in particular implies that the wind forcing of the depth-averaged flow is negligible compared with the JEBAR forcing. From (21) it follows that the following condition must be verified:

$$\max\left[\frac{H_0}{H_x} \mathbf{z} \cdot (\nabla \times \tau)_0, \tau_0^y\right] \ll \rho_0 (\chi_y)_0. \quad (27)$$

In (27), $\hat{\mathbf{z}} \cdot (\nabla \times \tau)_0$ and τ_0^y are characteristic values for the curl and the alongslope component of τ_s, respectively, H_0 is a characteristic value for the bottom depth, and $(\chi_y)_0$ is a characteristic value for the alongslope PE gradient. At the same time, the alongslope component of the wind-driven Ekman transport must be small when compared to that of the total transport so that from (19)

$$\frac{\tau_0^x}{f_0\rho_0} \ll (\Psi_x)_0, \tag{28}$$

where f_0 and τ_0^x are characteristic values for the Coriolis parameter and the cross-slope component of τ_s, respectively.

Over a steep continental slope one expects the topography effects to be much more important than the meridional advection of planetary vorticity. In our particular domain geometry where there can be no cross-slope transport and no associated stretching, this implies that the JEBAR predominates over the β effect. For a given potential energy gradient such a condition leads to an upper limit value for the alongslope transport:

$$(\Psi_x)_0 \ll \frac{H_x}{\beta_0 H_0}(\chi_y)_0, \tag{29}$$

where β_0 is a characteristic value for the alongslope gradient of the Coriolis parameter.

Applying the simplifications (24)–(26) and (28) to the momentum equation (19) leads to the following equations for the cross- and alongslope components of the velocity outside the Ekman layers ($\delta_E = 0$):

$$u = u_r' - \epsilon v_r' + \mu\left(\frac{\Psi_x}{H} - \overline{v}_r\right), \tag{30a}$$

$$v = \frac{\Psi_x}{H} + v_r'. \tag{30b}$$

In (30a,b), the simplifications appropriate for the slope region have resulted in the omission of all frictional terms except for the terms proportional to ϵ and μ in the equation for u. In the bottom friction term one recognizes the expression for the alongslope component of the geostrophic bottom velocity, the second part of this term being just the depth-averaged geostrophic velocity relative to the bottom, which arises as a correction to the depth-averaged flow. The internal friction term, $\epsilon v_r'$, on the other hand, depends on the vertical structure of the alongslope velocity.

As a final step, one has to postulate a form of the density distribution. We here assume a linear alongslope distribution:

$$\rho_y = b, \tag{31}$$

where b is uniform over the domain. One should note that, since b is uniform, both horizontal components of the geostrophic flow (14) are uniform along the slope. Relation (31) is used in (13) to get a simple expression of the cross-slope component of the geostrophic shear velocity:

$$u_r' = \frac{d}{f}(2z + H), \tag{32}$$

where $d = 0.5bg/\rho_0$. It is also used in (10) to obtain a simple expression for the alongslope gradient of χ:

$$\chi_y = -dH^2. \tag{33}$$

Applying the simplifications (22), (24), (27), (29), and (33) to the vorticity equation (21) yields the following simplified equation for the streamfunction of the depth-integrated flow:

$$-\chi_y(H^{-1})_x = \left[\epsilon f\frac{\Psi_x}{H}\right]_x + \left[\mu f\left(\frac{\Psi_x}{H} - \overline{v}_r\right)\right]_x. \tag{34}$$

As expected, the above equation indicates a balance between a forcing term on the left-hand side, the JEBAR, and a damping term on the right-hand side due to internal (first term) and/or bottom (second term) friction. Dissipation of vorticity at the bottom is only achieved by the alongslope component of the bottom flow since, according to (15) and (33), there is no alongslope velocity shear associated with the cross-slope bottom velocity $u_b = -\overline{u}_r$.

Equations (30a,b) together with (34) yield the solution to the problem provided that (34) can be integrated across the slope. At the slope base, the contribution of the relative flow, $\overline{v}_r|_{x=L_c}$, will be estimated from data. For convenience, we write the barotropic flow there as

$$\left.\frac{\Psi_x}{H}\right|_{x=L_c} = s\overline{v}_r|_{x=L_c}, \tag{35}$$

where s is an unknown constant factor. The alongslope bottom velocity at the slope base, $v_b|_{x=L_c}$, is therefore modeled as $(s-1)\overline{v}_r|_{x=L_c}$. For the present application, if not stated differently, s will be set to 1 so that $v_b|_{x=L_c} = 0$.

c. The resulting flow velocity

The model solution is obtained by solving the vorticity equation (34) and introducing the result for the depth-averaged alongslope flow into (30a) and (30b). Therefore, the solution is strictly valid for the interior flow outside the surface and bottom friction layers. Hereafter, the expressions for the flow characteristics at the surface (bottom) should be regarded as estimates just below (above) the corresponding Ekman layers. Using (33) and (35), the cross-slope integration of (34) yields

$$\frac{\Psi_x}{H} = v_p + \frac{\mu}{\epsilon + \mu}\overline{v}_r + v_{\text{boundary}}, \tag{36}$$

where

$$v_p = \frac{d}{f}\frac{H_b - H}{\epsilon + \mu} \tag{37}$$

is the JEBAR induced part of the flow, hereafter referred to as the primary flow, and

$$v_{\text{boundary}} = \frac{s\epsilon + (s-1)\mu_b}{\epsilon + \mu}\overline{v}_r|_{x=L_c}, \tag{38}$$

where $\mu_b = r/fH_b$ is the contribution due to the flow at the boundary.

Inserting (36) into (30b) yields the final expression for the alongslope velocity:

$$v = v_p + v_s \tag{39}$$

in which

$$v_s = v_r - \frac{\epsilon}{\epsilon + \mu}\overline{v}_r + v_{\text{boundary}} \tag{40}$$

is the complementary depth-dependent part of the flow, hereafter referred to as the secondary flow. The alongslope components are linked by the following relation:

$$v_p + v_s = v_b + v_r. \tag{41}$$

Using (36) and (40), the cross-slope velocity (30a) can be rewritten as

$$u = u_p + u_s, \tag{42}$$

where the primary and secondary parts are defined as

$$u_p = u_r' + \mu v_p \tag{43}$$

with u_r' given by (32), and

$$u_s = -\epsilon v_s + (\epsilon + \mu)v_{\text{boundary}}. \tag{44}$$

The terminology ''primary'' or ''secondary'' used above does not refer to different orders of magnitude for the corresponding flows. Instead, the primary and the secondary flows are related to the alongslope and cross-slope density gradients, respectively. Under the present model assumptions, the gradients in these two directions are uncoupled making the two flows independent of each other. In terms of driving mechanisms, the alongslope density gradient controls the shear component, u_r', of the cross-slope velocity and, through a vertically integrated effect (the JEBAR), the entire alongslope primary flow v_p. When bottom friction exists, the JEBAR also contributes to a part of the cross-slope primary flow u_p.

d. The primary flow

Equations (37) and (43) show that both the alongslope and the cross-slope components of the primary flow are controlled by dissipation. However, the cross-slope flow can only feel the effect of dissipation if both internal and bottom friction coexist together. The direction of the flow along the slope is entirely determined by the sign of the PE gradient along this slope while the direction of the cross-slope flow also depends on the hemisphere.

The alongslope component of the primary flow v_p is depth independent and, for a given PE gradient, decreases for increasing values of the friction coefficients. The velocity magnitude increases from zero at the base of the slope to a maximum value over an isobath $H_{v\text{-max}}$ located on the upper half of the slope. The exact cross-slope distribution of the alongslope component of the flow depends on the magnitude of friction and, more specifically, $H_{v\text{-max}}$ only depends on the relative magnitude of μ_b with respect to ϵ. Then $H_{v\text{-max}}$ can be written as

$$\begin{cases} H_{v\text{-max}} = \left\{\left[\dfrac{\mu_b}{\epsilon}\left(1 + \dfrac{\mu_b}{\epsilon}\right)\right]^{1/2} - \dfrac{\mu_b}{\epsilon}\right\}H_b, & \epsilon \neq 0 \\ H_{v\text{-max}} = \dfrac{1}{2}H_b, & \epsilon = 0, \end{cases} \tag{45}$$

that is ranging from 0 (for $\mu_b = 0$) to $H_b/2$.

The alongslope transport achieved by a water column of unit width,

$$V_p = v_p H = \frac{d}{f}\frac{(H_b - H)H}{\epsilon + \mu}, \tag{46}$$

has a different cross-slope distribution from the velocity. Compared with $H_{v\text{-max}}$, the maximum transport is moved downslope over the isobath $H_{V\text{-max}}$ defined as

$$\begin{cases} H_{V\text{-max}} = \dfrac{1}{4}\left\{1 - 3\dfrac{\mu_b}{\epsilon} + \left[\left(1 - 3\dfrac{\mu_b}{\epsilon}\right)^2 + 16\dfrac{\mu_b}{\epsilon}\right]^{1/2}\right\}H_b, & \epsilon \neq 0 \\ H_{V\text{-max}} = \dfrac{2}{3}H_b, & \epsilon = 0, \end{cases} \tag{47}$$

that is ranging from $H_b/2$ (for $\mu_b = 0$) to $2H_b/3$.

The cross-slope component of the primary flow, u_p, is depth dependent with a linear vertical distribution. The zero crossing along the vertical is found at the depth z_c defined as

$$z_c = -\frac{H}{2} - \frac{\mu}{\epsilon + \mu}\frac{H_b - H}{2}. \tag{48}$$

It only exists downslope of $H_{v\text{-max}}$. The modulus of u_p is maximum at the surface and, if $\mu = 0$, is also maximum at the bottom. The surface velocity,

$$u_p|_{z=0} = \frac{d}{f}\left[H + \frac{\mu}{\epsilon + \mu}(H_b - H)\right], \tag{49}$$

is, when $\epsilon = 0$, uniform and equal to $u_c = dH_b/f$. In all other friction regimes, it varies across the slope with

TABLE 1. Expressions for the different components of the alongslope transport for a general case where both types of friction coexist ($\mu_0 \neq 0$ and $\epsilon \neq 0$) and for the two limit cases of purely internal ($\mu = 0$) and purely bottom ($\epsilon = 0$) friction.

Transport	($\mu_0 \neq 0$ and $\varepsilon \neq 0$)	$\mu_0 = 0$	$\varepsilon = 0$
Primary	$T_p = \frac{d}{f}\frac{H_b^2 L_c}{6}\frac{1}{\varepsilon}\left\langle 1 - \frac{3}{2}\frac{\mu_0}{\varepsilon}\left\{1 + \frac{\mu_0}{\varepsilon}\left[1 - \left(1 + \frac{\mu_0}{2\varepsilon}\right)\ln\left(1 + \frac{2\varepsilon}{\mu_0}\right)\right]\right\}\right\rangle$	$T_p = \frac{d}{f}\frac{H_b^2 L_c}{6}\frac{1}{\varepsilon}$	$T_p = \frac{d}{f}\frac{H_b^2 L_c}{6}\frac{1}{\mu_0}$
Secondary	$T_s = \int_0^{L_c} \frac{\mu\overline{v}_r + [s\varepsilon + (s-1)\mu_b]\overline{v}_r\vert_{x=L_c}}{\varepsilon + \mu} H\, dx$	$T_s = s\frac{H_b L_c}{2}\overline{v}_r\vert_{x=L_c}$	$T_s = T_r + (s-1)\frac{H_b L_c}{3}\overline{v}_r\vert_{x=L_c}$
Bottom	$T_b = T_p - \int_0^{L_c} \frac{\varepsilon\overline{v}_r - [s\varepsilon + (s-1)\mu_b]\overline{v}_r\vert_{x=L_c}}{\varepsilon + \mu} H\, dx$	$T_b = T_p - T_r - s\frac{H_b L_c}{2}\overline{v}_r\vert_{x=L_c}$	$T_b = T_p - (s-1)\frac{H_b L_c}{3}\overline{v}_r\vert_{x=L_c}$
Relative	$T_r = \int_0^{L_c} \overline{v}_r H\, dx$		

a modulus that never exceeds u_c. The near-bottom velocity,

$$u_p|_{z=-H} = -\frac{d}{f}\left[H - \frac{\mu}{\epsilon + \mu}(H_b - H)\right], \quad (50)$$

varies across the slope in all cases. If $\mu = 0$, it is exactly opposite to the surface velocity. The cross-slope transport associated with a water column of unit width,

$$U_p = \frac{d}{f}\frac{\mu}{\epsilon + \mu}(H_b - H)H = \mu V_p, \quad (51)$$

vanishes in accordance with (24) if $\mu = 0$. If some bottom friction exists, U_p is nonzero, except at the coast and at the slope base, and must be compensated by the Ekman transport associated with the primary flow, $U_{pE} = -\mu V_p$, as can be verified by combining (12) and (16).

Since only u_p is depth dependent, the primary flow must turn with depth. The vertical turning is given by

$$\phi_z = -\frac{v_p u_{pz}}{(u_p^2 + v_p^2)} = \frac{2\gamma}{(2z + H - \gamma\mu)^2 + \gamma^2} \approx \frac{2}{\gamma}, \quad (52)$$

where ϕ is the direction of the flow (positive counterclockwise) and $\gamma = (H - H_b)/(\epsilon + \mu)$. The sign of the turning is therefore independent of the alongslope potential energy gradient. A detailed analysis of (52) shows that the approximate depth independence of ϕ_z holds everywhere across the slope except close to its margins. This baroclinically induced turning may be called the JEBAR turning and can be parallelled with the β spiraling (Schott and Stommel 1978) or with the turning induced by a wind stress having a component parallel to the topography (none of these mechanisms is considered here).

The most remarkable consequence of switching off one of the two modes of friction is the modification of the vertical velocity. Writing the continuity equation (3) for the primary flow and integrating from the surface to a depth z outside the bottom Ekman layer yields the vertical velocity associated with this flow:

$$w_p = -zu_{px} = -z\frac{d}{f}H_x\left[1 - \frac{\mu(\epsilon H_b + \mu H)}{(\epsilon + \mu)^2 H}\right]. \quad (53)$$

It is therefore the internal friction that allows vertical velocities in the primary flow. Extending the vertical integration of (3) down to the bottom of the Ekman layer and substituting for $w|_{z=-H}$ using the boundary condition (5) yields

$$w_p|_{z=-H} - w_e - w_t = 0. \quad (54)$$

In (54), $w_p|_{z=-H} = Hu_{px}$ is given by (53), while $w_e = -(U_{pE})_x$ is the Ekman suction velocity due to the divergence of the bottom Ekman transport and $w_t = -H_x u_p|_{z=-H}$ is the topographic stretching velocity associated with the primary flow. In case internal friction is ignored, $w_p|_{z=-H} = 0$ and one can check that w_e and w_t should compensate for each other while, if $\mu = 0$, there is no Ekman flow and the near-bottom vertical velocity is just the topographic stretching velocity.

e. The alongslope transports

The general expressions for the different components of the alongslope transport as well as the corresponding expressions in the limit friction cases where $\mu = 0$ or $\epsilon = 0$ are given in Table 1. The primary transport has been written in terms of the bottom friction parameter estimated at midslope, $\mu_0 = 2\mu_b$, so that a symetric dependence of T_p on the friction parameters ϵ and μ_0 can be found in the corresponding limit cases, $\mu_0 = 0$ and $\epsilon = 0$.

The primary and the secondary transports, T_p and T_s, are found by vertical and cross-slope integration of (37) and (40) while the transport T_b associated with the bottom velocity is deduced from

$$T_b = T_p + T_s - T_r, \quad (55)$$

where T_r is the geostrophic transport relative to the bottom. In order to estimate the secondary, the relative, and the bottom transports the cross-slope distribution of the geostrophic transport relative to the bottom, $H\overline{v}_r$,

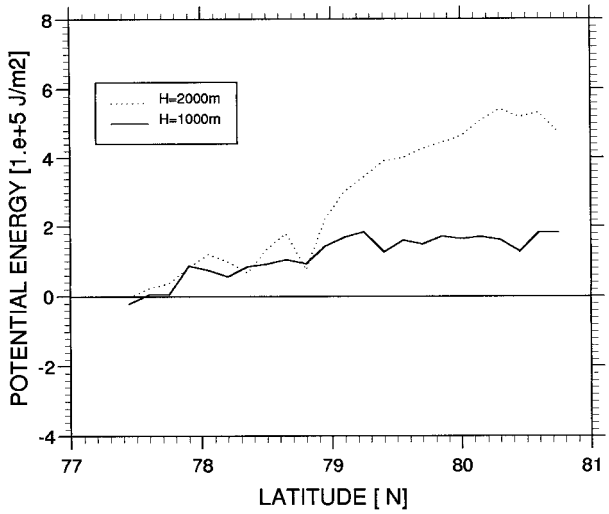

FIG. 4. Alongslope distribution of the PE anomaly of the whole water column (in 10^5 J m^{-2}) following the 1000-m (solid line) and the 2000-m (dotted line) isobath deduced from the MIZEX 84 observations approximately from 77.4°N to 80.8°N. The anomaly has been calculated with respect to the PE associated with the mean vertical density profile in Fram Strait.

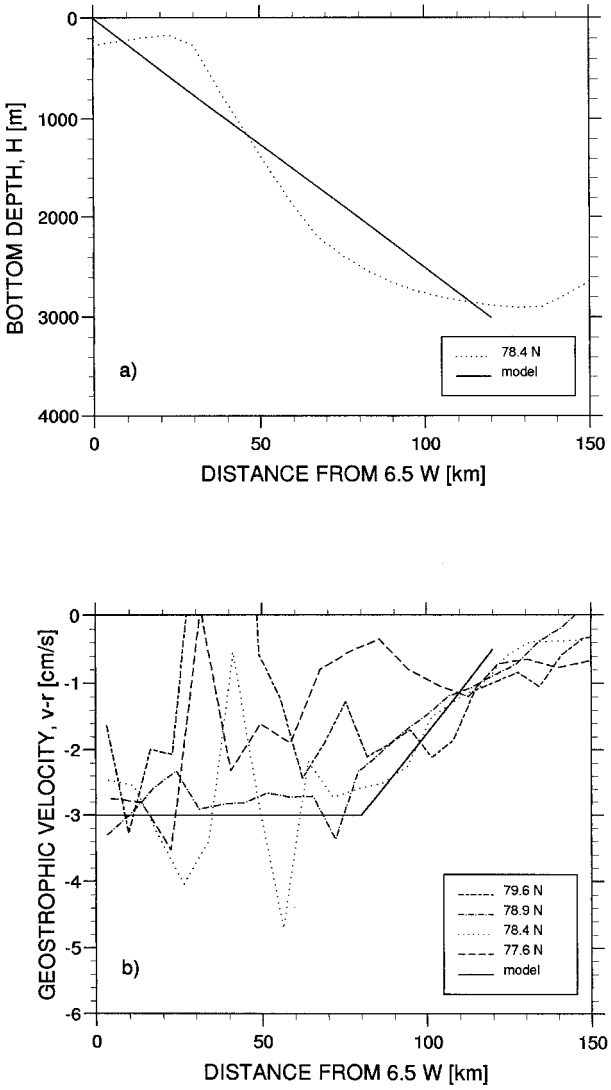

FIG. 5. Cross-slope distribution of (a) the observed bottom depth at 78.4°N (dotted line) and its model estimate (solid line) and (b) the model depth-averaged alongslope geostrophic velocity referred to the bottom (solid line) and the depth-averaged meridional geostrophic velocity referred to the bottom estimated from the MIZEX 84 data at 77.6°N (dashed line), 78.4°N (dotted line), 78.9°N (dotted-dashed line), and 79.6°N (dashed line with alternating long and short dashes). The observed distributions extend from 6.5°W eastward, over a distance of 150 km, slightly beyond the eastern model boundary (120 km).

needs to be known. A distribution of $\overline{v}_r$ consistent with the MIZEX 84 data is postulated as explained in the next section.

4. Determination of model parameters

From the MIZEX 84 data, a northward large-scale along-isobath gradient of PE is found over the East Greenland slope between 77.4° and 80.8°N (Fig. 4). The corresponding parameter relevant for the JEBAR, d in (33), has therefore a negative sign leading to a southward flow. From a linear least squares fit of the curves in Fig. 4, d is estimated to be between -5.1×10^{-10} s^{-2} for $H = 1000$ m and -3.5×10^{-10} s^{-2} for $H = 2000$ m. A characteristic value of $d = -4.5 \times 10^{-10}$ s^{-2} has been chosen for the present study.

The topographic parameters of the model, the depth at the slope base H_b, and the slope width L_c are set to 3000 m and 120 km. In Fig. 5a, the model topography is compared with the observed bottom depth profile along 78.4°N. The western boundary of the model domain (6.5°W) corresponds to the origin of the cumulated relative-to-bottom geostrophic transport shown in Fig. 3. The eastern boundary of the model slope has been chosen as a compromise so that it approximately coincides with both the observed slope base and the location of the maximum of the observed transport at the same latitude. More precisely, the location of the eastern boundary is such that the observed relative transport within the limits of the model domain is exactly 4 Sv. The real bottom slope is steeper and narrower than its model equivalent but the two topographies roughly provide the same cross-sectional area.

A uniform distribution of the relative-to-bottom depth-averaged alongslope geostrophic velocity $\overline{v}_r$ is postulated over the upper portion of the slope, and a linear distribution outward:

$$\overline{v}_r = a_1, \qquad 0 \le x \le L_r, \tag{56a}$$

$$\overline{v}_r = \overline{v}_r|_{x=L_c} + a_2(H - H_b), \qquad L_r \le x \le L_c, \tag{56b}$$

where

$$a_2 = \frac{\overline{v}_r|_{x=L_c} - a_1}{H_b(1 - L_r/L_c)},$$

and the coefficient a_1 as well as the distance L_r are estimated from data so that the relative transport T_r associated with $\overline{v}_r$ in the model is 4 Sv. The distribution of $\overline{v}_r$ along 78.4°N corresponding to the velocity section in Fig. 2d, and its model equivalent based on Eqs. (56a,b), are shown in Fig. 5b. Note that, despite the global agreement, differences between model and observations may be locally large, up to 2 cm s^{-1}. However, as also shown in Fig. 5b, these differences along the selected latitude 78.4°N are within the range of the alongslope variations of $\overline{v}_r$ observed between 77.6° and 79.6°N. In particular, the velocity distribution at 78.9°N, where the ratio 1:1 between the relative and the bottom transport has been postulated by Foldvik et al. (1988), very much resembles the approximated velocity profile used in the model.

The choice of the friction parameters is constrained by the requirement that both friction parameters ϵ and μ should be small [Eqs. (7) and (18)]. We choose 0.1 as an upper limit for both the parameter ϵ and the bottom friction parameter at midslope, μ_0. For $\mu_0 < 0.1$, condition (18) is verified everywhere across the slope except in a band close to the coast where H tends to zero. Either friction parameter should be significantly larger than the cross-slope Rossby number $R_u = U_0 f_0^{-1} L_c^{-1}$, a condition necessary for neglecting in (1) the nonlinear advection of alongslope momentum with respect to the corresponding friction force. For $f_0 = 1.4 \times 10^{-4}$ s^{-1} and taking $U_0 = 2 \times 10^{-2}$ m s^{-1} as the characteristic cross-slope velocity, one obtains $R_u \cong 10^{-3}$. Other dynamical assumptions provide upper limits for the magnitude of the velocity, which can be changed into lower limits on the friction parameters using the relation between velocity and friction provided by the model. Neglecting the alongslope momentum advection term with respect to the Coriolis term in (1) leads to a condition on the alongslope Rossby number, $R_v = V_0 f_0^{-1} L_c^{-1}$; that is, $R_v \ll 1$ or, equivalently, to the condition $V_0 \ll 17$ m s^{-1} for the alongslope velocity. Approximating $(\Psi_x)_0$ by $H_0 V_0$ in order to rewrite (29) as $V_0 \ll dH_x \beta_0^{-1}$ and taking $\beta_0 = 4.4 \times 10^{-12}$ m^{-1} s^{-1}, one obtains the more stringent condition $V_0 \ll 2.5$ m s^{-1}. If V_0 is considered to be the depth-averaged velocity at midslope, then the distribution plotted in Fig. 6 provides the necessary limits for a combination of the friction parameters. Allowing for V_0 to be one order of magnitude smaller than the above value of 2.5 m s^{-1} leads to a limit of about 0.02 for $(\epsilon + \mu_0)$, comparable with the limit imposed by the value of R_u given above.

The resulting envelope of friction parameters, that is, $\epsilon < 0.1$, $\mu_0 < 0.1$, and $(\epsilon + \mu_0) > 0.02$, allows the alongslope velocity to vary by a factor 3 or 4 (Fig. 6) and the total transport to take values between 7 Sv and 31 Sv (Fig. 7d, see section 5a).

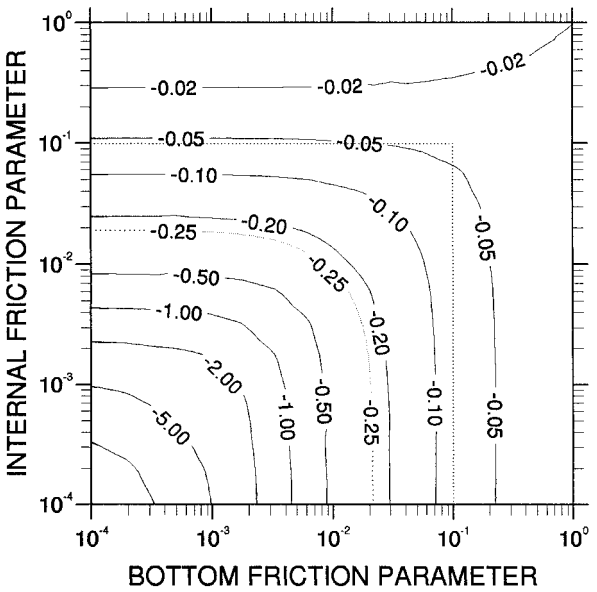

FIG. 6. Depth-averaged total alongslope velocity at midslope (in m s^{-1}) as a function of the bottom (μ_0) and internal (ϵ) friction parameters. The dotted isoline corresponds to the upper limit for the velocity while the dotted lines of constant μ_0 and ϵ correspond to the upper limits for these friction parameters as discussed in the text.

5. Model results

a. The transports in the EGC

The primary, the secondary, the bottom, and the total transports are presented in Figs. 7a–d in the space of the friction parameters ϵ and μ_0. The dotted lines in this figure mark the upper and lower limits of the allowable range of friction parameters defined in section 4. In agreement with the density distribution observed during MIZEX 84, the primary and the secondary transports are both southward so that the total transport is southward as well. Since the relative transport T_r is prescribed in the model, the shape of the distributions of the bottom (Fig. 7c) and total (Fig. 7d) transports is the same and only the values differ, with the total transport larger by 4 Sv than the bottom transport.

The magnitude of the JEBAR forcing [d in Eq. (33)] is an external parameter of our model. Under the assumption of a balance between JEBAR and friction, this forcing entirely determines, for a given amount of total friction, the magnitude of the alongslope component of the JEBAR-induced portion of the barotropic flow (the primary flow). This is clearly evident from the shape of the isolines of T_p in Fig. 7a, which is approximately the same as that of the isolines of the total friction parameter $(\epsilon + \mu_0)$. As a consequence, T_p takes large values as the amount of friction becomes small. Still, T_p will never exceed 30 Sv or be smaller than 6 Sv, as required by the limits on the friction parameters.

For the present application with $s = 1$, the secondary transport, T_s, can be shown to be the sum of the relative

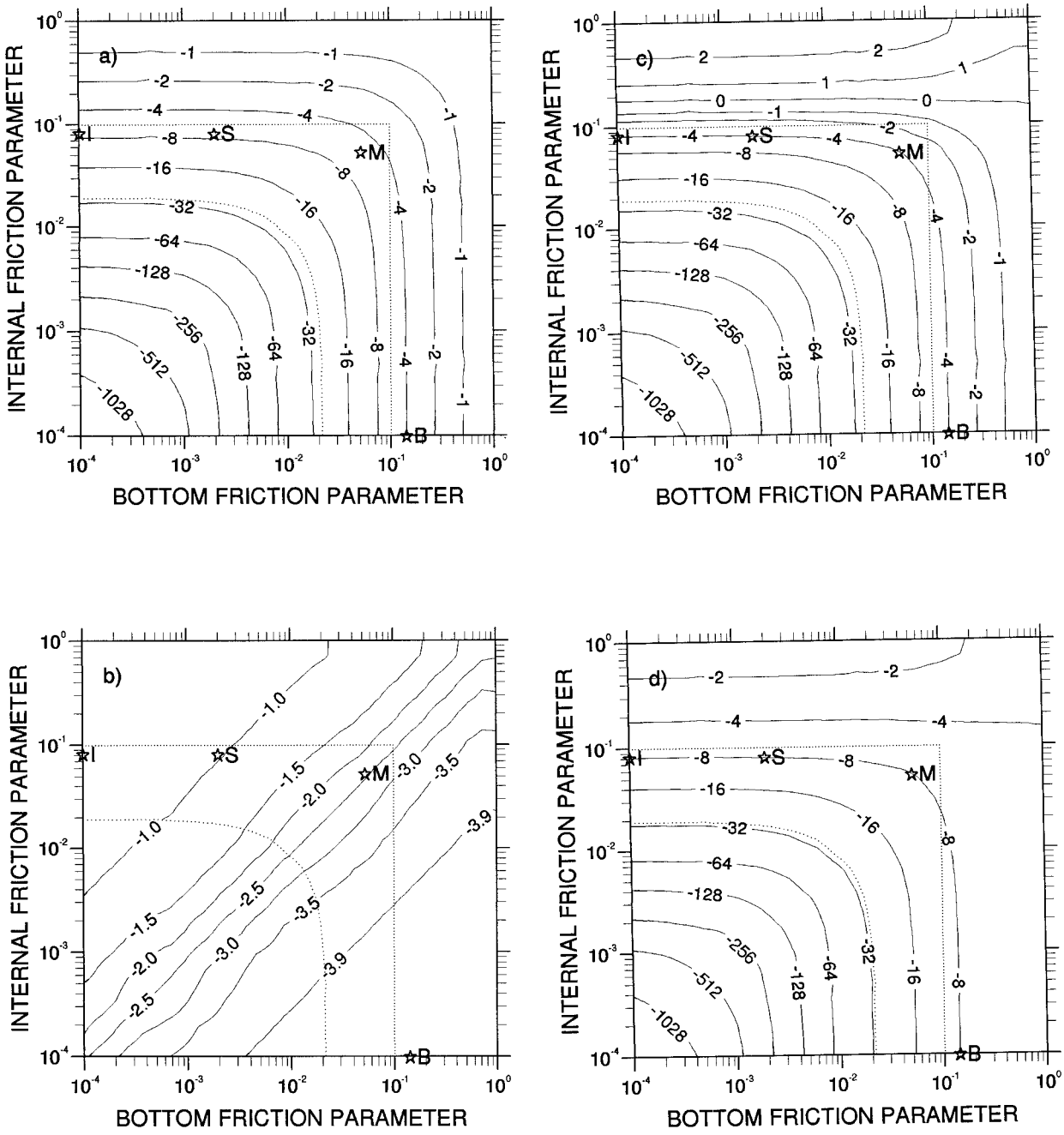

FIG. 7. Total alongslope volume transport (in 10^6 m^3 s^{-1}) as a function of the bottom (μ_0) and internal (ϵ) friction parameters associated with (a) the primary flow, (b) the secondary flow, (c) the bottom flow, and (d) the total flow. The dotted lines mark the limits of model validity. The points I, S, M, and B correspond to the particular friction regimes discussed in the text. The points I and B have been moved onto the actual limits of the plot although they correspond to $\mu_0 = 0$ and $\epsilon = 0$, respectively.

transport T_r plus a contribution dependent on the boundary condition term at the slope base (Table 1). Both $\overline{v}_r$ and the boundary condition are prescribed as external inputs to the model (see section 4). The added contribution depends upon a fraction of $(\overline{v}_r|_{x=L_c} - \overline{v}_r)$, which is positive and has a smaller magnitude than $\overline{v}_r$ for the model velocity profile shown in Fig. 5b. Therefore, the magnitude of T_s cannot exceed that of T_r, that is, 4 Sv. The actual magnitude of the added contribution depends on the relative importance of the internal and bottom frictions and vanishes if internal friction is ignored. Therefore, T_s can be approximated by a function of the

ratio ϵ/μ_0, as demonstrated by the shape of the isolines in Fig. 7b, and reaches its upper limit in the purely bottom friction regime. The larger ϵ/μ_0, the smaller the magnitude of the secondary transport. For $\epsilon/\mu_0 > 30$, T_s is smaller than 1 Sv and T_p is practically function of ϵ alone (upper-left corner of Figs. 7a and 7b). The lower limit, $T_{sl} = 0.9$ Sv, is obtained in the purely internal friction regime ($\mu_0 = 0$). On the contrary, for $\epsilon/\mu_0 < 0.03$, T_s retains more than 97.5% of T_r (3.9 Sv) and T_p is a function of μ_0 alone (lower-right corner of Figs. 7a and 7b).

The secondary transport represents that part of the total transport not directly controlled by the JEBAR forcing. For cases corresponding to the same JEBAR forcing and the same amount of total friction ($\epsilon + \mu_0$), the magnitude of the total flow therefore only depends on the relative importance of the bottom and internal frictions. In the present context where T_r is fixed, differences in the total flow are entirely attributed to differences in the bottom flow and must be explained by the different adjustment of the latter to the two types of friction. As the relative importance of the internal friction increases, it is the entire water column, rather than the bottom flow, that adjusts to the JEBAR forcing through friction. In regimes close to the purely internal friction regime ($\epsilon/\mu_0 > 30$), the JEBAR-induced flow is distributed between the relative-to-bottom (T_r) and the bottom (T_b) flow and explains the entire current transport (if one excepts a small contribution of the secondary flow through the boundary term T_{sl}). The contribution of the JEBAR forcing to the bottom flow, and therefore the bottom flow itself, are then minimum. Conversely, the larger the relative importance of the bottom friction, the larger the contribution of T_b to the total transport as the JEBAR influence is more restricted to the bottom flow. This can be deduced from a comparison of Figs. 7c and 7a, where close to the purely bottom friction regime ($\epsilon/\mu_0 < 0.03$), the isolines of T_b coincide almost exactly with the isolines of T_p. In this case, the bottom flow-contribution is maximum and is just the JEBAR-induced flow. The above remarks can also explain the varying impact of increasing the total amount of friction depending on the friction regime. In regimes close to purely internal friction, such an increase would tend to cancel out the total transport, that is, provided sufficient internal friction exists in the system, T_b could in principle vanish and even reverse sign (Figs. 7c,d). However, such a reversal is not possible within our allowable range of friction parameter values (Fig. 7c) where T_b is southward and the minimum value of the total transport is not less than 7 Sv. In regimes close to purely bottom friction, increasing the total amount of friction would tend to increasingly dissipate the JEBAR-induced vorticity through bottom friction and therefore to cancel out the bottom flow, leaving the relative-to-bottom flow as the only contribution to the total transport. However, considering the amount of friction allowed by the model, such a situation would not occur since T_b cannot fall below 6 Sv (Fig. 7c, bottom-right corner).

TABLE 2. Values of the friction parameters ϵ and μ_0 for the four friction regimes discussed in the text, all leading to a 4 Sv bottom geostrophic transport in the EGC, and the corresponding values of the primary (T_p) and secondary (T_s) transports.

Region	Acronym	ϵ	μ_0	T_p (Sv)	T_s (Sv)
Internal	I	0.079	0.000	7.1	0.9
Special	S	0.078	0.002	7.0	1.0
Mixed	M	0.048	0.048	5.6	2.4
Bottom	B	0.000	0.141	4.0	4.0

In the remainder of section 5, the model results are further analyzed for selected regimes defined by different combinations of the friction prameters corresponding to the same bottom transport value of 4 Sv, that is, to the most realistic value of T_b in the EGC (see section 2). Four regimes have been explored: the purely internal friction regime (I regime) defined by $\mu_0 = 0$, the purely bottom friction regime (B regime) for which $\epsilon = 0$, a mixed friction regime (M regime) for which the friction parameters are equal, and a special friction regime (S regime) for which μ_0/ϵ is small but nonzero (see Table 2 and Figs. 7a,b for the values of the friction parameters and of the transports T_p and T_s in these regimes). Note that the value of μ_0 in the B regime is slightly larger than the upper limit ($\mu_0 = 0.1$) selected for this parameter in section 4. Since both the upper limit for μ_0 and the selected value for T_b are somehow arbitrary, the B regime can still be considered a plausible one at this stage of the analysis.

b. The flow structure

1) THE PURELY INTERNAL FRICTION REGIME

In the I regime, the alongslope primary velocitiy v_p has a linear cross-slope distribution with values decreasing from about 12 cm s^{-1} at the coast to 0 at the slope base (Fig. 8a). The maximum of the alongslope transport V_p occurs at midslope and is about 90 m^2 s^{-1} (Fig. 8b). The contribution of the secondary flow to the total alongslope velocity is, in this regime, equal to the alongslope component of the geostrophic baroclinic shear, $v_r - \overline{v}_r$, plus a contribution from the boundary condition [Eq. (40)]. The former disappears upon vertical integration while the latter, for $s = 1$ in (38), is uniform across the slope and equal to $\overline{v}_r|_{x=L_c} = 0.5$ cm s^{-1}. Therefore, the contribution of the secondary flow to both the total depth-averaged velocity, $\overline{v}$ (Fig. 12a), and the transport, V (Fig. 12b), is negligible except close to the slope base.

In the I regime, the cross-slope velocity u_p has also a linear cross-slope distribution but is much smaller than v_p. At the surface, it is directed upslope and increases from 0 at the coast to less than 1 cm s^{-1} at the slope base (Fig. 9a). At the bottom, u_p has equal magnitude but opposite direction when compared with the surface

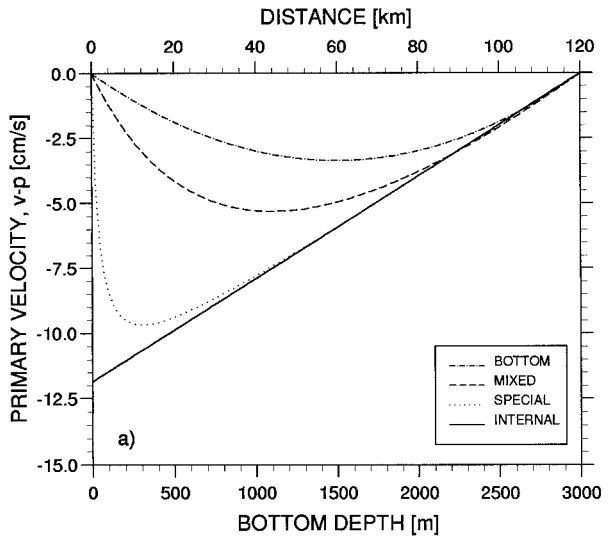

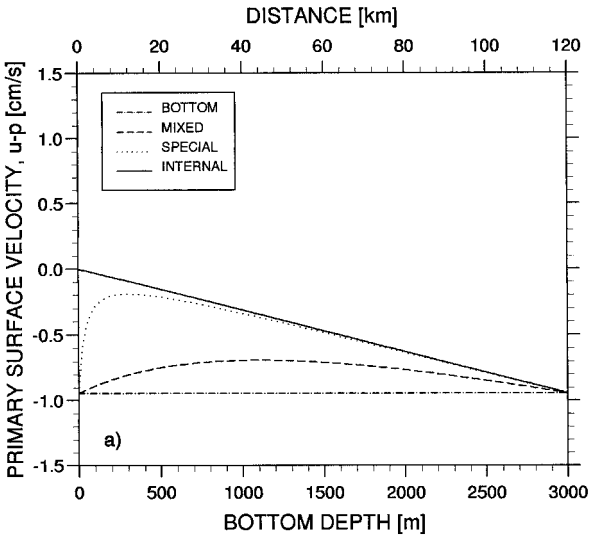

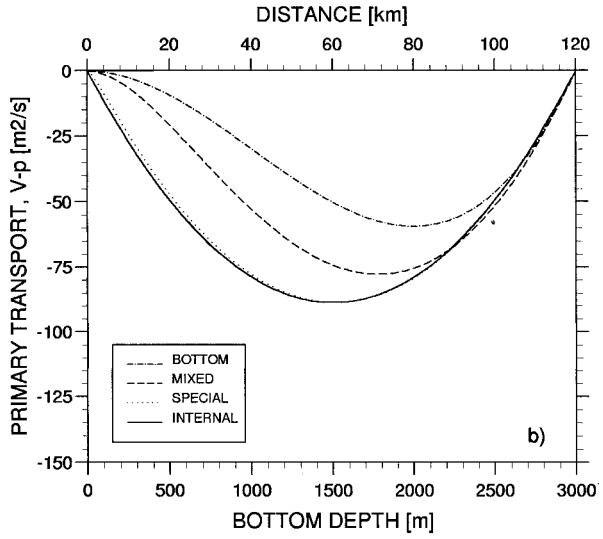

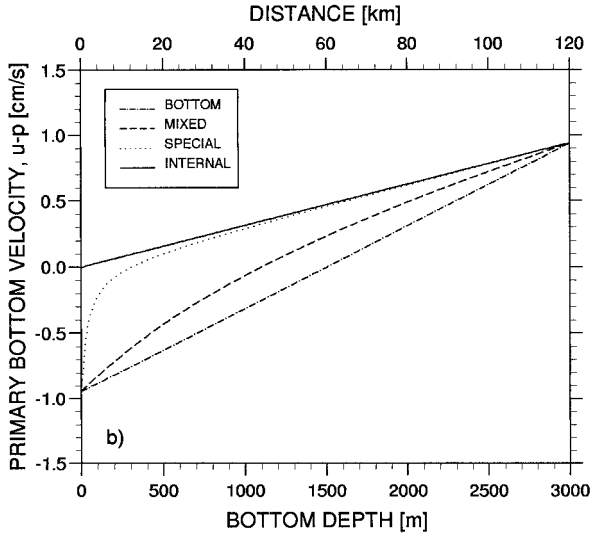

FIG. 8. Cross-slope distribution of (a) the alongslope velocity component (in 10^{-2} m s^{-1}) and (b) the transport per unit width (in m^2 s^{-1}) associated with the primary flow for four friction regimes: I regime (solid line), S regime (dotted line), M regime (dashed line), and B regime (dot-dashed line). See explanation in the text.

FIG. 9. Same as Fig. 8 except cross-slope (a) surface and (b) bottom velocity component (in 10^{-2} m s^{-1}).

velocity (Fig. 9b). As a result, the horizontal primary flow turns clockwise from the bottom toward the surface. The turning increases as the inverse of the distance to the slope base, from a value of about 4×10^{-5} rad m^{-1} at the coast (Fig. 11a). The change of sign of u_p along the vertical occurs at middepth ($z_c = -H/2$) everywhere across the slope (Fig. 10a) and results in a zero cross-slope transport U_p (Fig. 10b). There is no contribution of the secondary flow to the cross-slope transport either, as can be checked upon vertically integrating (44) after inserting (40). These equations also show that the cross-slope secondary velocity u_s has a zero-crossing at the level where $v_r = \overline{v}_r$. Since v_r in the EGC is southward and decreases with depth throughout the whole water column (Fig. 2d), u_s is directed offshore (onshore) in the upper (lower) layer. Therefore, the direction of u_s is opposite to that of its primary counterpart, both at the surface and at the bottom. At the surface, its magnitude (not shown here) is larger than that of u_p (except close to the slope base) so that the cross-slope flow direction is dictated by the secondary flow. At the bottom, however, u_s is larger than u_p only in the upper quarter of the slope (Figs. 9b and 13b).

As the gradient of PE has a northward component, the vertical velocity of the primary flow, w_p, is downward in the I regime. It increases linearly from zero at the surface to a maximum at the bottom, which, according to (53), becomes larger as one gets closer

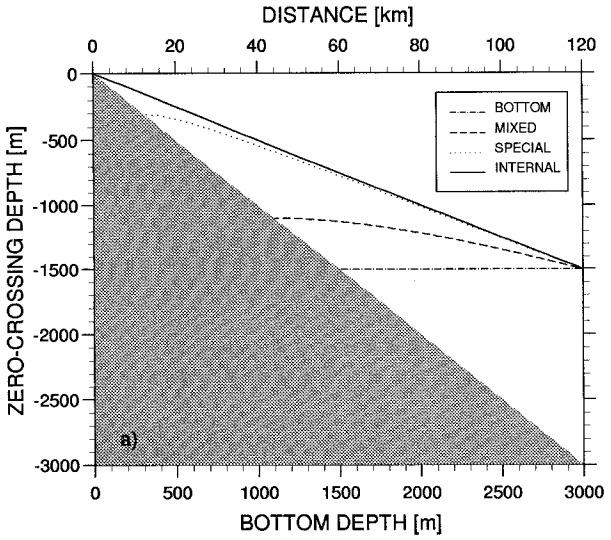

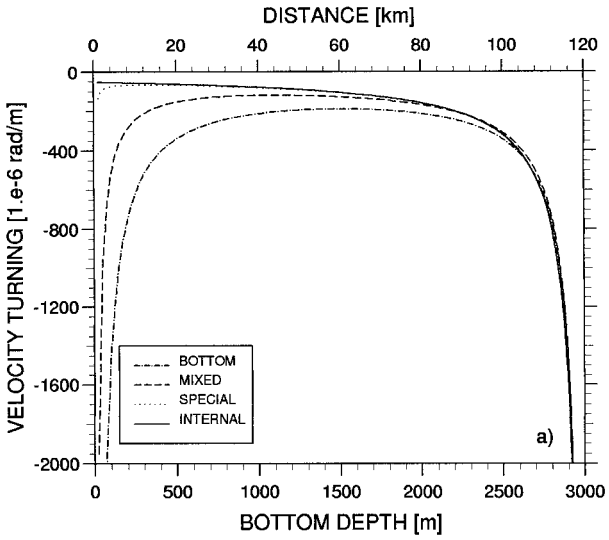

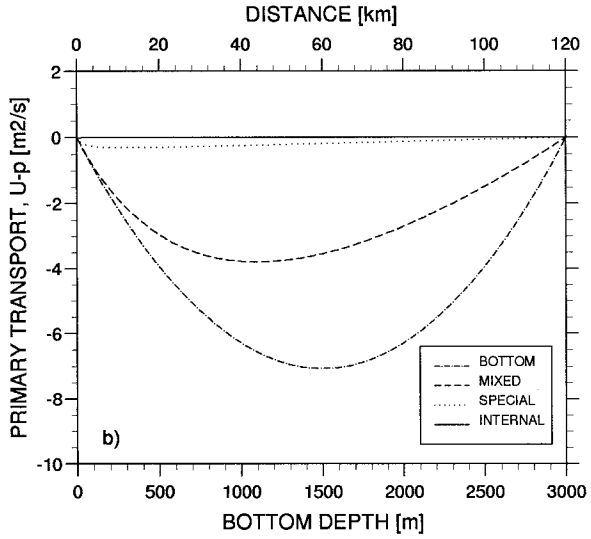

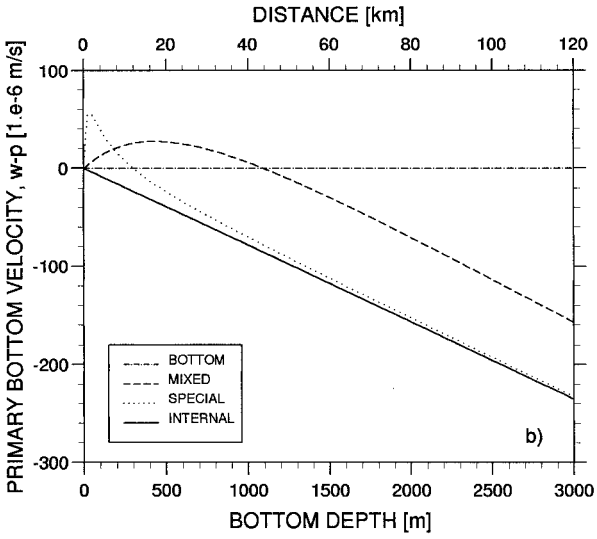

FIG. 10. Same as Fig. 8 except (a) depth (in m) of the zero-crossing of the cross-slope velocity component and (b) cross-slope transport per unit width (in $m^2\ s^{-1}$).

FIG. 11. Same as Fig. 8 except (a) approximate clockwise turning of the horizontal velocity (in 10^{-6} rad m^{-1}) [see Eq. (52)] and (b) vertical velocity at the bottom (in 10^{-6} m s^{-1}). Negative values indicate clockwise rotation as one moves upward in the water column.

to the slope base, reaching there 2.5×10^{-4} m s^{-1} (Fig. 11b). At this location, w_p represents nearly the total vertical velocity at the bottom since the secondary cross-slope velocity, which has the same cross-slope structure as $\overline{v}_r$ ($v_r = 0$ at the bottom), decreases to a negligible value at the slope base. The contribution of the secondary flow to the vertical velocity at the bottom can be neglected from the slope base up to midslope where u_s does not exceed $u_p/2$ (Figs. 9b and 13b).

2) THE PURELY BOTTOM FRICTION REGIME

In the B regime, the cross-slope distribution of the alongslope primary velocity is parabolic with the maximum southward velocity at midslope (Fig. 8a). The maximum velocity is 3.5 cm s^{-1}, that is, approximately one-third of the maximum velocity in the I regime, which occurs at the coast. However, in the B regime, v_p represents only the bottom velocity since $v_s = v_r$ [Eqs. (40) and (38)]. Adding the contribution of the secondary flow would bring the maximum of the depth-averaged alongslope velocity to a value nearly twice as large (Fig. 12a). In comparison to the I regime, the maximum of the primary and total transports, V_p and V, is moved downslope to $H = 2H_b/3$ (Figs. 8b and 12b). The maximum of V is approxi-

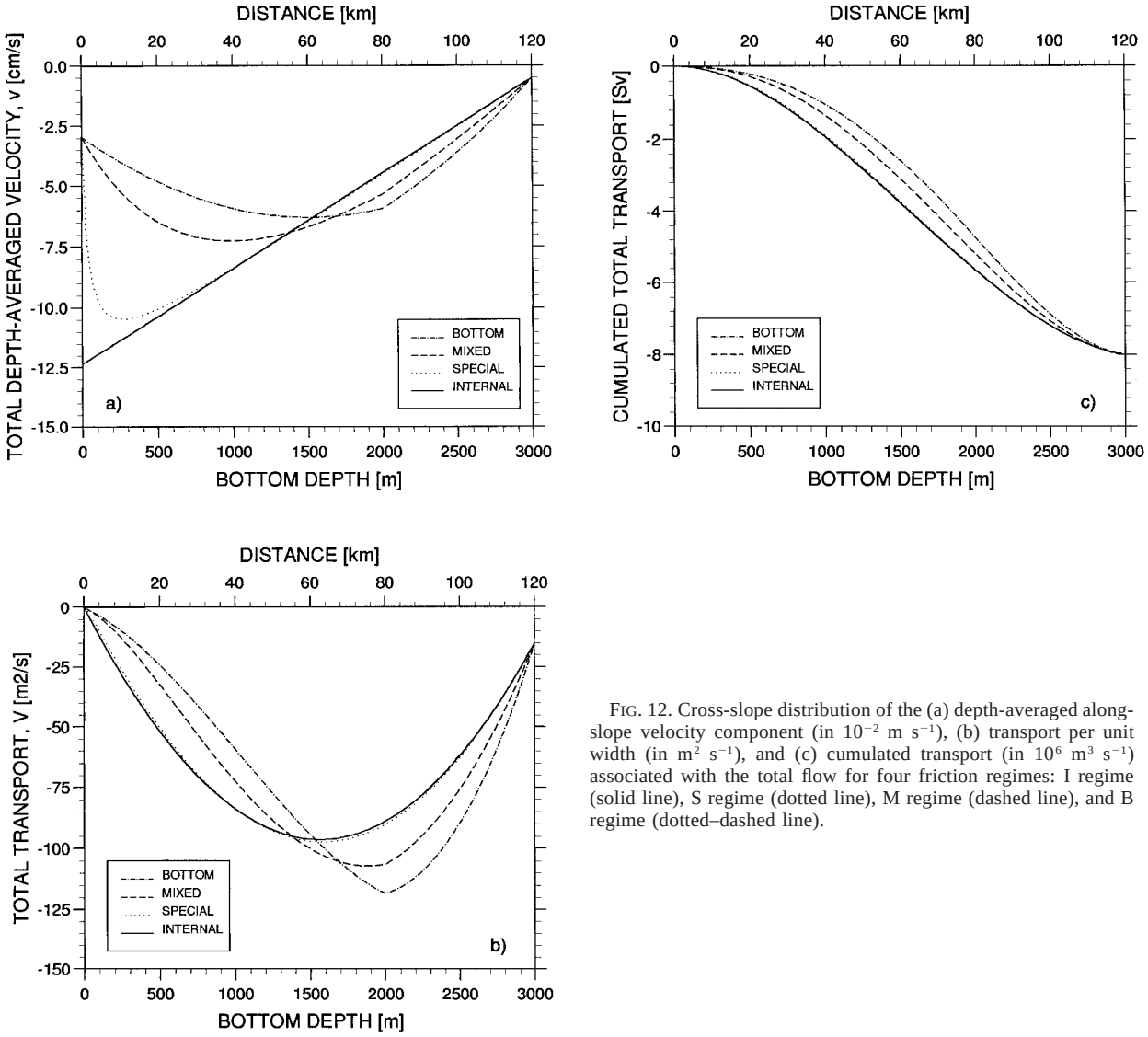

FIG. 12. Cross-slope distribution of the (a) depth-averaged alongslope velocity component (in 10^{-2} m s^{-1}), (b) transport per unit width (in m^2 s^{-1}), and (c) cumulated transport (in 10^6 m^3 s^{-1}) associated with the total flow for four friction regimes: I regime (solid line), S regime (dotted line), M regime (dashed line), and B regime (dotted–dashed line).

mately 120 m^2 s^{-1}, that is, twice as large as the maximum of V_p, and exceeds by about 20% the maximum in the I regime.

In the B regime, $u_s = 0$ [Eqs. (38) and (44)] so that u_p is the total cross-slope velocity. At the surface u_p is directed upslope, as in the I regime, but its magnitude is independent of the position across the slope, being everywhere equal to the maximum value in the I regime (Fig. 9a). Since the depth of the zero-crossing, $z_c = -H_b/2$, is also independent of the position (Fig. 10a), the bottom cross-slope velocity is directed upslope over the shallowest part of the slope and downslope over the deeper part (Fig. 9b). The resulting onshore transport, U_p, is nonzero and has a parabolic cross-slope distribution with a maximum of 7 m^2 s^{-1} at midslope (Fig. 10b), that is about 6% of the maximum total alongslope transport (Fig. 12b). Such a distribution of u_p also results in a clockwise turning of the primary velocity vector upward, with a minimum at midslope where it is twice as large as the turning at the same location in the I regime (Fig. 11a).

Since the bottom Ekman transport U_{pE} is opposite to U_p, it is directed downslope. The Ekman vertical velocity w_e is downward upslope from the maximum of U_{pE} and upward downslope from it. It exactly balances the vertical velocity w_t caused by the topographic vortex stretching [Eq. (54)] so that the vertical velocity w_p is everywhere zero (Fig. 11b). As expected, there is no vertical motion associated with the secondary flow, either. Moreover, since $u_s = 0$ and $v_s|_{z=-H} = 0$, the topographic stretching and the Ekman transport due to this flow vanish separately.

3) THE MIXED FRICTION REGIME

In the M regime, the effects of the internal and bottom frictions have to be considered altogether. For any regime with both types of friction, there exists a location where $\mu = \epsilon$. Since μ is inversely proportional to H, the bottom friction dominates upslope of this location while, downslope from it, the internal friction dominates. In our particular M regime ($\epsilon = \mu_0$) this location is at midslope. Around this location, the flow characteristics take intermediate values between the B and the I regime. For instance, the distribution of the alongslope velocity v_p coincides with the distribution in the I regime over the lower one-third of the slope, exhibits a maximum of about 5.5 cm s^{-1}, at $H_{v\text{-max}} \approx H_b/3$, and then drops to zero at the coast as in the B regime (Fig. 8a). The maximum of the total alongslope velocity, $\overline{v}$ (Fig. 12a), as for v_p, is located at $H_{v\text{-max}}$ but its magnitude is 35% larger due to the added contribution of the depth-averaged secondary flow, $\overline{v}_s$. In fact, $\overline{v}_s$ is maximum (equal to 3 cm s^{-1}) at the coast where it is just the relative flow velocity, $\overline{v}_r$. The maximum alongslope transport, V_p, amounts to nearly 80 m^2 s^{-1} and is located between the corresponding maxima in the I and B regimes, that is, between $H = H_b/2$ and $H = 2H_b/3$ (Fig. 8b). In the vicinity of this maximum, the secondary flow contribution to the alongslope transport amounts to about 35 m^2 s^{-1} (Fig. 12b).

In the M regime, the cross-slope primary velocity u_p is directed upslope at the surface as in the above limit regimes but has a different cross-slope distribution. For instance, it has a minimum equal to 0.7 cm s^{-1} at $H = H_{v\text{-max}}$ (Fig. 9a) as can be found from (49). At the same location, one finds the limit of the outer slope region where a zero crossing exists in the vertical profile of u_p (Fig. 10a) and where the bottom value of u_p changes sign (Fig. 9b). This location also corresponds to the maximum of the onshore transport U_p [cf. Eqs. (37) and (51)] and to the minimum of the clockwise turning rate of the horizontal velocity vector [cf. Eqs. (37) and (52)], each entremum being about half the corresponding value in the B regime (Figs. 10b and 11a, respectively). The vertical velocity w_p at the bottom is upward (downward) upslope (downslope) of this location (Fig. 11b). As in the B regime, the topographic stretching velocity w_t is always opposite to the Ekman velocity w_e. However, the former everywhere dominates over the latter (except at the coast where the two are equal) so that the vertical velocity of the primary flow has the same sign as the topographic vortex stretching but a different distribution. From the distributions of u_p at the bottom and of U_p one can deduce that both w_t and w_e have a zero-crossing at $H = H_{v\text{-max}}$ and magnitudes that increase from this location to maximum values at the coast and at the slope base. Adding the two distributions yields a maximum of w_p located between the coast and $H = H_{v\text{-max}}$, approximately at $H = 400$ m. The secondary flow also modifies, but to a smaller extent than in the I regime, the cross-slope characteristics of the flow.

4) THE SPECIAL FRICTION REGIME

A peculiar characteristic of the purely internal friction regime is the maximum of the alongslope primary velocity v_p being located at the coast. Inclusion of a small amount of bottom friction, like in the S regime, removes this feature (Fig. 8a). In this latter regime, the bottom friction dominates over the upper 380 m of the slope area. As a result, v_p in the S and I regimes coincide only over the deeper two-thirds of the slope and diverge over the remaining upper part. The difference between velocities at $H = 380$ m is still small (about 1.5 cm s^{-1}), but increases rapidly farther upslope as v_p in the S regime undergoes an abrupt decrease to 0 toward the coast. Because the difference in the distributions of v_p between the S and I regimes is mainly concentrated over the shallowest part of the slope, a difference in the alongslope transport, V_p, is hardly detected in any part of the slope (Fig. 8b). Similarly, the primary transport T_p only changes by 1.5% between the two regimes (Table 2) so that the S regime is close to the I regime as far as transports are concerned.

As in the I regime, the secondary alongslope velocity and transport are small in the S regime. For instance, the maximum velocity $\overline{v}$ (Fig. 12a) is only 1 cm s^{-1} greater than the maximum v_p (Fig. 8a). Similarly, the maximum V_p (Fig. 8b) is more than 90% of the maximum total transport V (Fig. 12b), both located very close to midslope, at $H = 1520$ m. The 0.1 Sv deficit of T_p in the S regime as compared with the I regime is distributed over the upper slope and is compensated by the secondary transport increase over the lower slope.

The differences and similarities identified in the alongslope flow more generally apply to the distribution of all flow characteristics in the S regime (Figs. 9–11 and 13). Basically, although the S regime remains quantitatively close to the I regime over most of the slope, with the exception of the area close to the coast, the distributions of the flow characteristics in this regime qualitatively resemble the corresponding distributions in the M regime. In particular, the distributions present an extremum or a zero-crossing at some distance from the coast, which arise because of the predominant influence of the bottom friction in the vicinity of the coast. The main difference with the M regime is in the position of these features since $H_{v\text{-max}}$ is moved upslope by 700 m, that is to 300 m (Fig. 8a).

6. Discussion

In section 5a, a value of 4 Sv for the bottom transport in the EGC in Fram Strait has been shown to be consistent with a simple frictional model in which the JEBAR is assumed to be the only explicit forcing for the barotropic flow. In section 5b, four particular friction

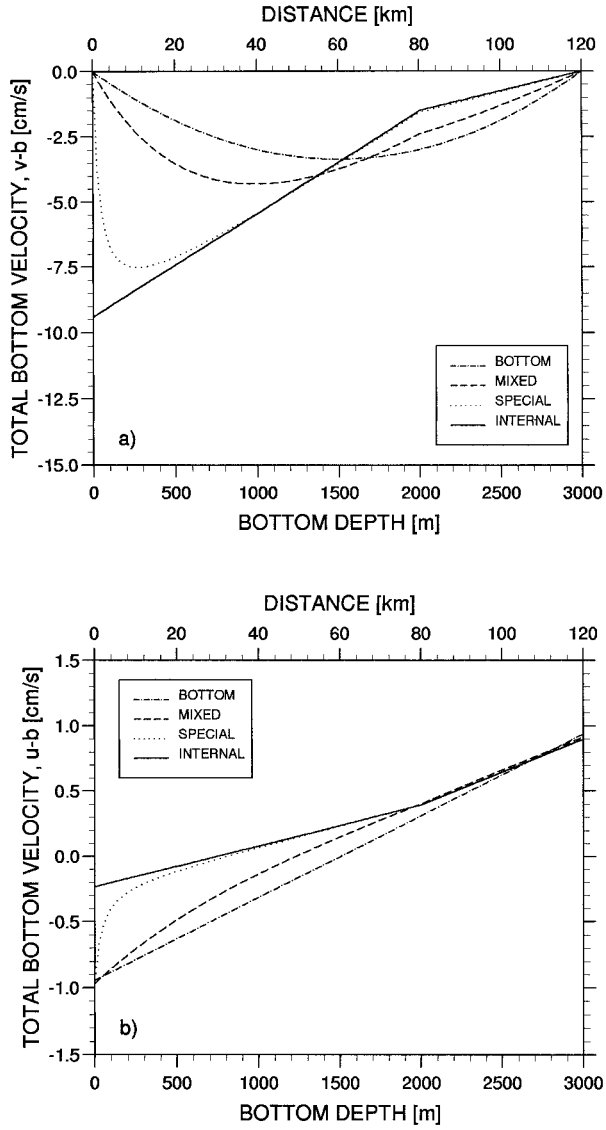

FIG. 13. Cross-slope distribution of the (a) alongslope and (b) cross-slope components of the bottom velocity (in 10^{-2} m s^{-1}) associated with the total flow for four friction regimes: I regime (solid line), S regime (dotted line), M regime (dashed line), and B regime (dotted–dashed line).

regimes have been investigated in details that illustrate the whole range of plausible regimes leading to this transport value. Although other values for the bottom transport, in the range from 3 Sv to 27 Sv, could be predicted by the model (Fig. 7c), the qualitative features related to either of the four regimes would not change. This section examines the a posteriori validity of the main model assumptions and analyses of the model flow characteristics against available data.

a. Validation of model assumptions

Other forcings than the JEBAR may drive a barotropic flow in the EGC in Fram Strait but the assumption of a predominance of the JEBAR appears to be justified, at least in summer, based on a scaling analysis using characteristic values provided by the model. For the wind stress forcing to be of comparable magnitude to the JEBAR forcing, either the wind stress curl should be of the order of 3×10^{-5} N m^{-3}, which would be equivalent to an Ekman pumping velocity of about 2×10^{-4} m s^{-1}, or the alongslope component of the wind stress should be at least 1 N m^{-2} [Eq. (27)]. Wind stress and wind stress curl estimates over the Greenland slope in Fram Strait, based on wind data from the Hindcast database of the Norwegian Meteorological Institute averaged over the period corresponding to the MIZEX 84 Experiment, are one order of magnitude smaller than the required minimum values mentioned above. Condition (28) for the cross-slope component of the wind stress is also satisfied according to the same data. Other possible forcings are likely to be negligible as well. Sea level gradients associated with the atmospheric pressure forcing would drive vertical velocities much smaller than those induced by the wind stress curl. The surface thermal forcing, on the other hand, is relatively weak in summer (Häkkinen and Cavalieri 1989) and is unlikely to produce significant vertical velocities at the base of the turbulent layer. Accounting for the presence of ice on top of the current may alter these estimates but will certainly not change the orders of magnitude.

The linear assumption for our model is guaranteed by a small Rossby number within the allowable range of friction parameters (see section 4). The steady-state assumption also appears to be valid since the timescales associated with the flow adjustment are small compared with the timescale over which the forcing (here the JEBAR) is assumed to be constant (typically the season corresponding to the period covered by the density observations). Adjustment can occur through friction with a characteristic timescale of order $T_* = (\epsilon_0 + \mu_0)^{-1} f_0^{-1}$, which, for a postulated bottom transport of 4 Sv, ranges between 12 and 24 h and, for a 27 Sv bottom transport, would be one order of magnitude larger. Adjustment by topographic waves would probably occur on similar timescales. For instance, Maslowski (1996) reported an alongslope component of the group velocity of about 4 m s^{-1} for a topographic wave generated over the Greenland Fracture Zone at 77°N and propagating along the East Greenland slope. Such a velocity would correspond to a travel time of about 24 h over a distance of 250 km.

Dissipative processes are represented in our model by linear friction laws both in the interior [Eq. (1)] and at the bottom [Eq. (16)], and only their alongslope components are retained. A Rayleigh type of friction in the interior is formally correct in a linear model (e.g., Salmon 1990). On the other hand, in the present context where the bottom velocity varies across the slope (Fig. 13a), a linear bottom stress based on a friction coefficient r uniform throughout the domain is perhaps difficult to justify. Moreover, if the present linear law was

to be considered an approximation to a more realistic quadratic law, an estimate of $C_D = r/|\mathbf{u}_b|$ using the maximum value of v_b across the slope would lead, in the B or M regimes, to unrealistically large values. In the S regime, however, C_D would be of the order of 5×10^{-3} at the maximum of the bottom velocity, indicating that the S regime may be the more realistic friction regime.

Assuming that the model physics are correct, there is still a large uncertainty in the model results linked to the choice of the friction parameters. For our selected value $T_b = 4$ Sv, ϵ and μ_0 are small enough to have both conditions (7) and (18) fulfilled over a major portion of the slope whichever friction regime is assumed to operate (Fig. 7c). Still, the predicted flow is no longer valid in a coastal zone where the local parameter μ is larger than 0.1, that is, upslope of $H = 20$ m and 100 m in the S and M regime, respectively. However, the cumulated transport in this zone can be expected to be negligible (Fig. 13c). In the B regime, μ is larger than 0.1 over most of the domain (down to $H = 2300$ m), which may invalidate this regime for the assumed transport. Similarly, as far as bottom friction is considered, the assumption that the cross-slope component of the friction force is negligible [Eq. (26)] is reasonable except for a narrow region in the vicinity of the coast. In the B regime, this region covers the shallower 20 km of the slope (Fig. 14c) and would become narrower as μ_0 decreases, that is, for increasing values of the bottom transport. In the purely internal friction regime, however, examination of the ratio $\epsilon u/v$ (Fig. 14a) shows that for reasonable values of $\epsilon < 0.1$, condition (25) is fulfilled at the surface everywhere across the slope while, at the bottom (Fig. 14b), a region exists near the base of the slope where the ratio may be locally fairly large. For $\epsilon = 0.079$, as chosen in our I regime, $\epsilon u_b/v_b$ exceeds 0.1 in the outer 20 km of the slope. In this area, the flow is not guided enough by the topography for the alongslope component of the flow to be larger than the cross-slope component. Rather the flow is more sensitive to the magnitude of the velocity prescribed at the boundary. This is demonstrated by Figs. 15a,b where the same ratios as in Figs. 14b,c are plotted for a modified boundary condition ($s = 2$). According to this condition, the alongslope bottom velocity at the slope base is forced to be equal to the depth-averaged relative geostrophic velocity $\overline{v}_r$ rather than to 0 as in the case $s = 1$. More substantial alongslope velocities are then induced inside the domain in the vicinity of the boundary so that the directionality of the flow is better ensured and condition (25) more easily satisfied. Although $s = 2$ may appear as a better boundary condition, it would, in any case, have a limited effect on the model results. Keeping the same values of the friction parameters as for $s = 1$, the same primary transport would be obtained. Only the total transport would change but by no more than about 10%. It should be also noted that, provided other assumptions are verified, the predicted barotropic component of the flow remains valid even in the areas where (25) or (26) are invalidated since none of these conditions has to be fulfilled for the vorticity equation of the depth-averaged flow (34) to hold. Errors in the local flow will not affect the flow in other areas [since only (34) makes the flow at any location dependent upon the flow downslope of the location] but may affect the cumulated transport.

The assumption (31) of a uniform alongslope density gradient can lead to additional errors in the predicted flow. This gradient, when estimated from the MIZEX 84 data, locally at 78.4°N or as an average from 77.4° to 80.8°N, is not uniform in the vertical with large values concentrated in a thin surface layer (0–200 m) and variations by more than one order of magnitude between the surface and the bottom. However, the vertical structures of ρ_y are similar over the 1000-m and 2000-m isobaths (Fig. 16) and are associated with values of $\chi_y/H^2 = -d$ differing by less than 25% from the estimates using the constant density gradient (see section 4). Therefore, the consequent error on the alongslope component of the primary flow v_p is also less than 25%. The same error also applies to the cross-slope component of the primary velocity at the bottom and at the surface since the contribution of the baroclinic velocity u_r' at these levels is proportional to the depth-averaged value of ρ_y (Eq. 13). However, since the model does not adequately reproduce the vertical structure of ρ_y, the vertical distribution of the cross-slope flow may be in error. Still, Fig. 16 indicates that, in the observations, ρ_y tends to keep the same sign throughout the whole water column, suggesting that the monotonic upward decrease of the primary cross-slope velocity predicted by our model may be a real feature.

Uncertainity in the model results may also be due to simplifications in the domain geometry. Although the mean depth of the model domain, $H_b/2$, and the location of the model slope base, L_c, are in good agreement with the observations at 78.4°N, local deviations of the linear cross-slope profile of the bottom depth from the real topography are substantial (see section 4). Moreover, the lateral extent of the slope and of the current varies with the latitude in Fram Strait (Fig. 1 and Fig. 5b, respectively). Nevertheless, the similarity between the cross-slope distributions of the depth-averaged relative velocity $\overline{v}_r$ at 78.4° and at 78.9°N (Fig. 5b), as well as between the associated transports, T_r, which are equal to about 4 Sv at both latitudes, suggests that the flow properties are roughly uniform along the slope at least over a distance of 60 km. In terms of total transport, this distance may even be larger since, in cases where internal friction dominates, the total transport is almost entirely controlled by the the alongslope PE gradient, which has been shown to be roughly uniform over a distance of 350 km.

b. Comparison with some other model results and observations

The importance of the JEBAR depends on the strength of the along-isobath gradient of PE, $\rho_o \chi_y$, which

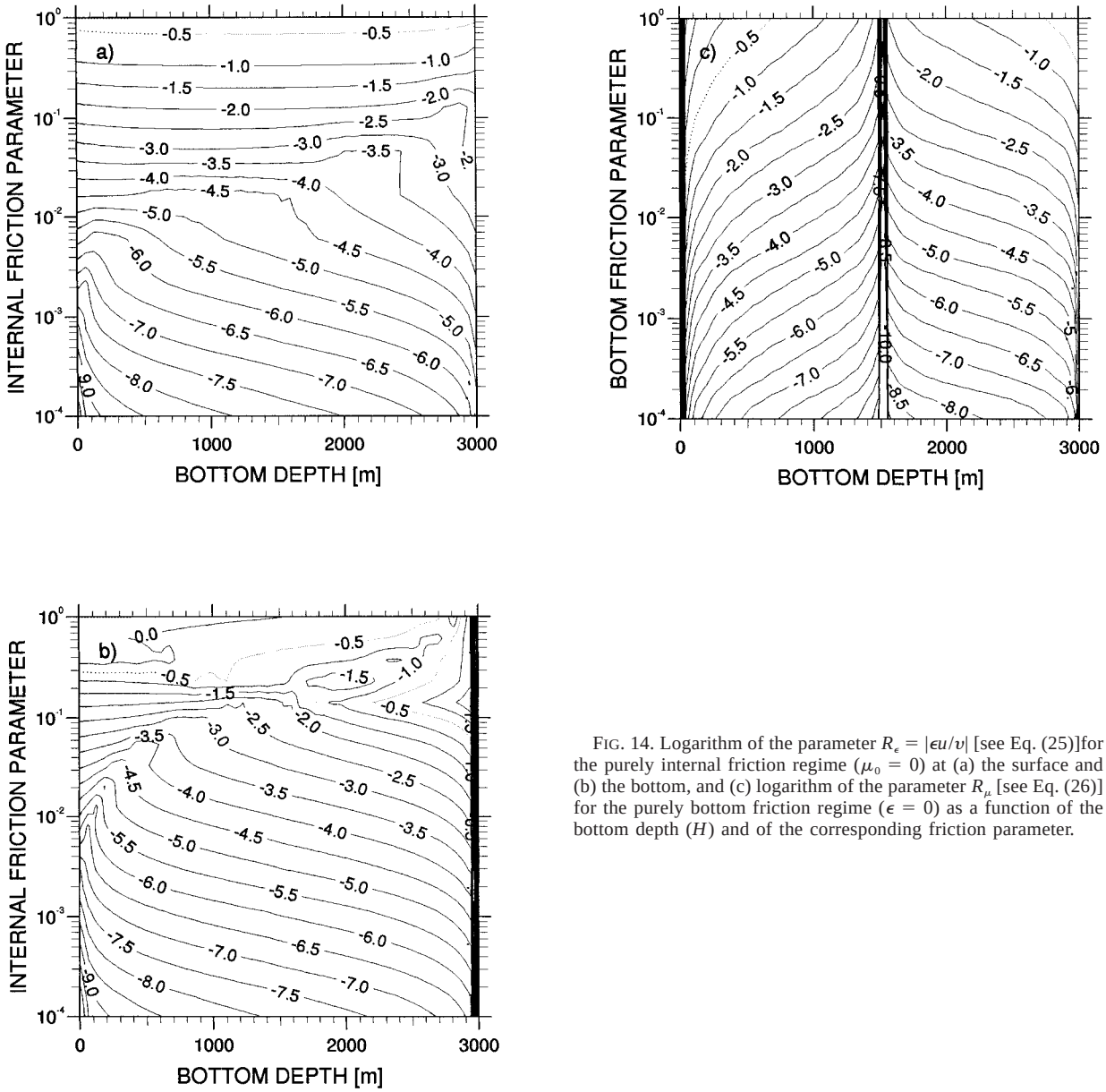

FIG. 14. Logarithm of the parameter $R_\epsilon = |\epsilon u/v|$ [see Eq. (25)]for the purely internal friction regime ($\mu_0 = 0$) at (a) the surface and (b) the bottom, and (c) logarithm of the parameter R_μ [see Eq. (26)] for the purely bottom friction regime ($\epsilon = 0$) as a function of the bottom depth (H) and of the corresponding friction parameter.

in the case of the EGC in Fram Strait has been estimated to be $0.45 \times 10^{-9}\ \rho_o H^2$ J m^{-3}. It is therefore of comparable magnitude with the PE gradient in other areas of the World Ocean. Huthnance (1984) reported values of χ_y/H^2 ranging from 0.2 to 1 ($\times 10^{-9}$ s^{-2}) depending on the considered slope current and demonstrated that such values are able to maintain a significant steady alongslope transport along the eastern oceanic margins.

The cross-slope variations of the density field add a baroclinic correction (which is called here the secondary flow) to the JEBAR-induced flow. In Huthnance's (1984) model, these variations are created through adjustment of the density field as determined by an advection–diffusion equation. By contrast, in the present model, the density distribution is prescribed from hydrographic data and cannot change through interaction with the induced velocity field. This approach does not necessarily lead to a larger error than Huthnance's since, in the EGC, the cross-slope hydrographic distributions are more certainly linked to the large-scale frontal structures and forcings associated with the EGPF rather than determined by the local advection field such as the one predicted by the model. As mentioned by Huthnance, the secondary flow may be responsible for substantial transports in currents with small lateral diffusion. This may not be the case in the EGC. For any friction regime

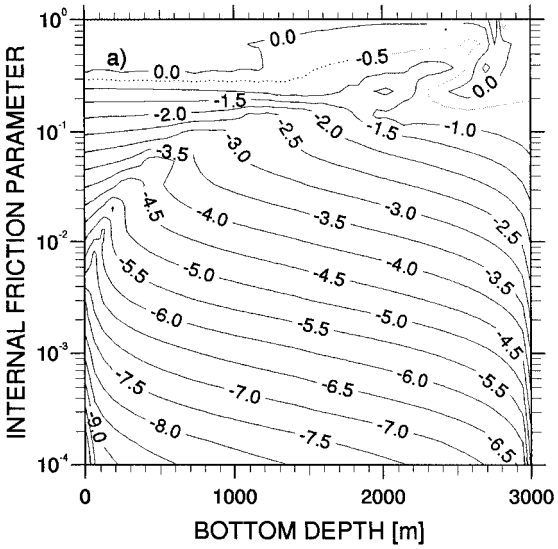

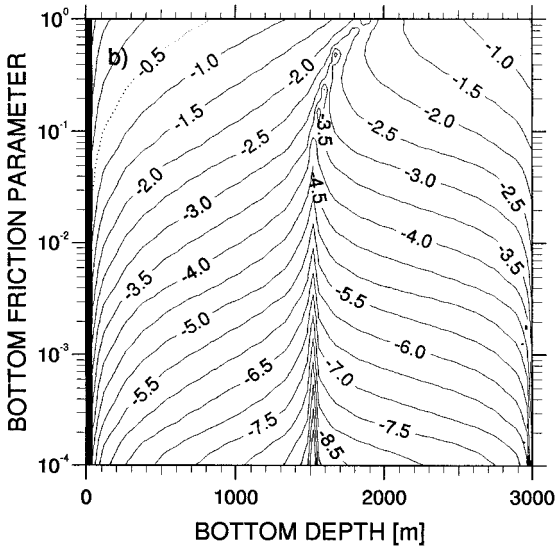

FIG. 15. Same as (a) Fig. 14b and (b) Fig. 14c except for the modified boundary condition ($s = 2$).

within the allowable range of our model, the ratio of the primary to the total transport never falls below 0.55 and, for regimes with large amount of internal friction, can be as large as 0.96 (Fig. 17). By including some internal friction, our model, by contrast with Huthnance's model, allows for a portion of the relative-to-bottom alongslope flow to be accounted for by the primary flow, therefore leading to larger values of this ratio. The predominance of the JEBAR flow in our model application is also evident from the similar cross-slope structures of the depth-averaged and primary velocities in the selected friction regimes (Figs. 12a and 8a).

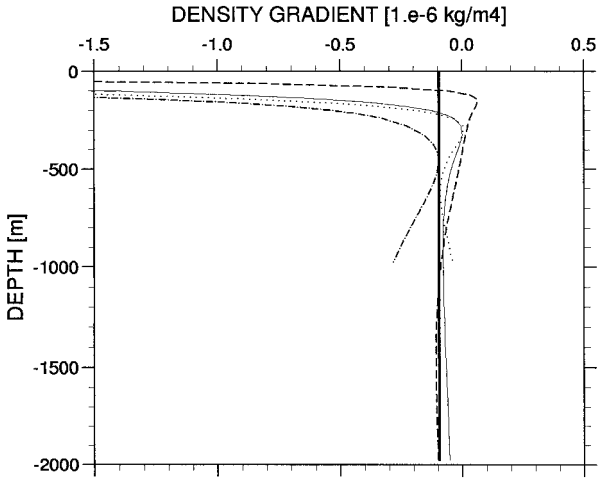

FIG. 16. Vertical distribution of the alongslope density gradient (in 10^{-6} kg m^{-4}) used in the model (bold solid line) together with its estimate from the MIZEX 84 data averaged from 77.4°N to 80.8°N over the 2000-m (light solid line) and the 1000-m (dotted line) isobath and obtained locally at 78.4°N over the 2000-m (dashed line) and the 1000-m (dotted–dashed line) isobath.

A remarkable feature of a JEBAR-driven current is the vertical turning of the horizontal velocity vector in any friction regime (Fig. 11a). This turning is clearly identified in the observations presented by Manley et al. (1987) (their Fig. 7) and has also been reported by Foldvik et al. (1988). In the latter case, the instruments moored at three different levels on three moorings revealed an upward clockwise turning at all moorings except at the shallowest one where the turning in the upper water column was anticlockwise but probably not significant. Although the turning given by (52) is associ-

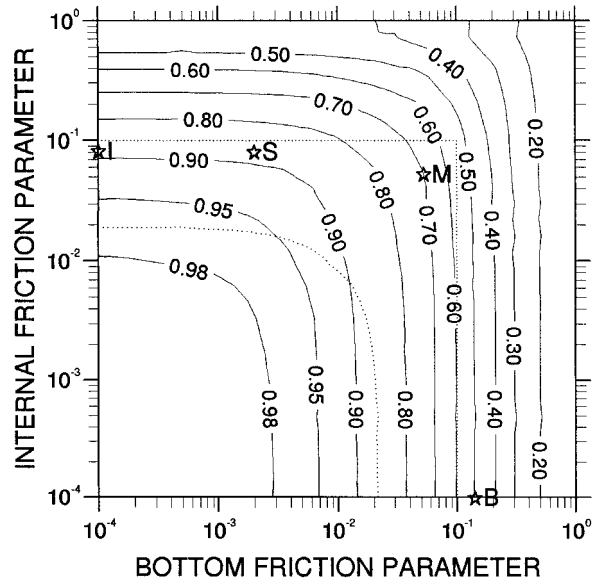

FIG. 17. Same as Fig. 7 except ratio of the primary to the total transport.

ated only with the primary flow, it is a good agreement with the observations. More generally, the vertical turning of the velocities, which may or may not be a signature of the JEBAR, appears to be a characteristic feature of the EGC all along the Greenland slope down to the Denmark Strait (Aagaard and Coachman 1968).

If the theoretical background of the model is to be believed, then the model results can be used to deduce information about the friction regimes in the EGC in Fram Strait. In particular, determination of the magnitude of the primary transport should allow one to assess the most plausible amount of total friction in the current. Based on a postulated total transport of 8 Sv, inferred independently from the observed relative-to-bottom transport and from Foldvik et al.'s (1988) results, a total friction parameter of approximately 0.08–0.14 has been chosen (section 5a). Since the selected value of 8 Sv may appear somewhat flexible, our choice for the total amount of friction should be separately validated through a comparison with the overall friction level in other similar slope currents. Along the western continental slope of the North Atlantic, Salmon and Ford (1995) showed that the northward excursion of the Gulf Stream can be reasonably predicted using a model with internal friction only and values of ϵ ranging between 0.015 and 0.04. In this range of values for ϵ, our model without bottom friction would predict a southward bottom transport between about 10 and 35 Sv. The value $\epsilon \approx 0.08$, which has been used in our model for the purely internal friction regime (I regime) and also for the regime with a small amount of bottom friction (S regime), is twice as large as the largest value of ϵ used by Salmon and Ford (1995), which rather corresponds to our mixed friction regime (M regime). Still, it is a reasonable estimate of ϵ, considering that these authors used the lower limit of ϵ required for model stability. On the other hand, if our model did not include any internal friction, then a relatively high bottom friction coefficient r should be used in order for the predicted transports to be reasonable. For instance, r is about 3 cm s^{-1} in the B regime, which should be compared with r in the range 0.01–0.1 cm s^{-1} used in similar studies (e.g., Huthnance 1984; Csanady 1985). The apparent discrepancy in the magnitude of friction can be explained by the comparatively deep water column in the EGC which makes more difficult dissipation of barotropic vorticity through friction. In our model, the JEBAR forcing is independent of the water depth while the corresponding dissipation depends primarily on the ratio $\overline{v}/H$. The range 0.01–0.1 cm s^{-1} for r corresponds to a value of μ_0 between 5×10^{-3} and 5×10^{-4}, and to a transport in the EGC, in the range 100–800 Sv, which lies outside the domain of validity of the model, essentially because condition (29) is invalidated. Considering that, in such low friction regimes, the dynamics are still linear ($R_\upsilon \ll 1$, see section 4), the behavior of the flow in these regimes can be extrapolated from the results obtained in the range of validity of the model. For small magnitudes of friction, another vorticity balance prevails in which both dissipation by friction and advection of planetary vorticity compete to cancel out the JEBAR-induced vorticity. Modifying (34) by adding a β term would therefore decrease the transport values mentioned above. Indeed, the vorticity sink associated with advection of planetary vorticity can be estimated in terms of an equivalent friction parameter, which, under the simplifications $\psi_{xx} = 0$ and $\overline{v}_r \ll \overline{v}$, can be scaled as $\mu_\beta = \beta_0 L_c / f_0$. A value of about 4×10^{-3} is obtained for this parameter, which is of the same order of magnitude as the largest of the aforementioned values for μ_0. Adding the two parameters, μ_0 and μ_β, to make up a friction term that compensates for the JEBAR would give a typical transport value of 60 Sv, which is still unrealistic. Therefore, within the limitations of a steady vorticity balance in which the JEBAR is a prescribed predominant forcing, a vorticity equilibrium with a large amount of friction ($\epsilon + \mu_0 \approx 10^{-2}$–$10^{-1}$) is the most plausible for the EGC in Fram Strait.

The question on the relative role of the bottom and of the internal friction in the EGC can be addressed by looking at barotropic vorticity budgets provided by regional models of the area. In the numerical model of Legutke (1991), the vertically integrated vorticity balance at 75°N over the East Greenland slope is achieved between the bottom torque and the contribution of the horizontal viscous terms parameterized by a standard shear viscosity. This would suggest that an equilibrium can exist in which internal friction dominates over bottom friction. However, over a sloping bottom, bottom friction in models with discrete topography is partly taken into account by the horizontal viscous terms so that its effect may be underestimated in Legutke's vorticity budget.

When comparing the model flow structures with observations, the purely internal friction regime does not appear very plausible since it predicts a maximum of the alongslope velocity at the coast (Fig. 8a). Therefore, some bottom friction is necessary, in particular in the shallowest part of the slope. Observations in the Ekman bottom layer could help to estimate the strength of the bottom friction but are unfortunately unavailable. At the surface, a comparison of the model velocity with direct observations is difficult since observations include a signal from forcings neglected in the model. Moreover, the cross-slope structure of the model alongslope surface velocity is relatively insensitive to the type of friction due to the surface intensification of the relative flow (Figs. 18a and 18b). Still, comparison of Fig. 2d with Fig. 18b (note that the cross-slope scale is different) shows that a sufficiently large bottom velocity (as in the S regime) results, in addition to a quantitative contribution to the main surface core of the EGC, in a secondary maximum of the surface velocity at the shelf break, which does not appear in the relative velocity field. Such a feature should be validated by observations. More instructive is a comparison based on the

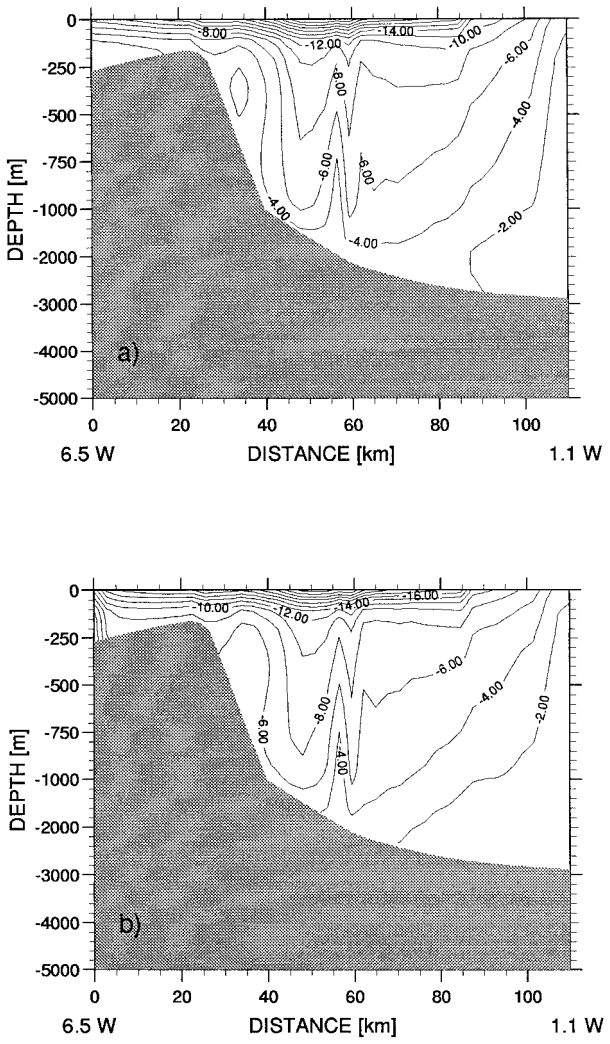

FIG. 18. Vertical distribution of the total alongslope geostrophic velocity (in 10^{-2} m s^{-1}) along the model section for (a) the B regime and (b) the S regime. Velocities are obtained by combining the model bottom velocity for the corresponding friction regime with the relative-to-bottom velocities deduced from the observations at 78.4°N as shown in Fig. 2d.

near-bottom velocity. Measurements at moorings located at 79°N (Foldvik et al. 1988) suggest that the southward component of the near-bottom velocity over the East Greenland slope increases upslope to a value of about 3 cm s^{-1} over the 1100 m isobath. An upslope increase, up to at least the 1100-m isobath, is also predicted by the model in either regime except the B regime (Fig. 13a). Moreover, the offshore component at 25 m above the bottom over the same isobath reported by Foldvik et al. (1988) is in agreement with a model regime where internal friction dominates (Fig. 13b). The possibility of a friction regime close to the I regime is also suggested by the good agreement between the value of 7 cm s^{-1} for the southward bottom velocity over the 1000-m isobath, obtained by substracting the relative velocities in Fig. 2d from Manley et al.'s (1987) current meter measurements (section 2), and the corresponding values of 5.5 cm s^{-1} predicted by the model in the S regime, or of 4.5 cm s^{-1} predicted in the M regime. Other regimes with larger bottom friction would give smaller values over the same isobath.

The above analysis shows that the limit cases of purely internal or purely bottom friction can be disregarded, while a mixed regime with comparable magnitude of the friction parameters or a regime with a relatively small amount of bottom friction are in good agreement with the observations of the alongslope velocities in the EGC in Fram Strait. Additionally, comparing the cross-slope velocities suggests that the most likely friction regime is the one with dominant internal friction.

7. Summary

The geostrophic, relative to the bottom, volume transport of the EGC at 78.4°N has been estimated from the MIZEX 84 hydrographic data collected in Fram Strait. The southward transport, estimated across a section 150 km long running from 6.5°W eastward is as large as 4.4 $\pm$ 0.5 Sv. The contribution of the polar water outflow from the Arctic Ocean is 0.8 Sv and the deep-water outflow amounts to 1.2 Sv. The remaining 2.4 Sv are due to the flow of Atlantic and Intermediate Water. Existing current meter data suggest that the geostrophic flow across the considered section at that time may have been associated with a bottom flow. We propose that such a bottom flow in the EGC in Fram Strait is due to the presence, over the East Greenland slope, of an alongslope gradient of potential energy, which is indeed identified in the MIZEX 84 data. Such a gradient represents a forcing, commonly known as the JEBAR, which generates a flow with a strong depth-independent alongslope component.

The JEBAR-induced flow has been investigated using an analytical model in which the bathymetry and the density distribution are idealized. The equations are written on the f plane and the dynamics are highly simplified. The JEBAR forcing is balanced by bottom and/or internal friction, both acting in the alongslope direction. The former is assumed to be a linear function of the near-bottom velocity while the latter is represented by a Rayleigh friction. The JEBAR forcing is shown to be responsible for a barotropic alongslope flow proportional to the potential energy gradient and inversely proportional to the strength of friction. The alongslope density gradient involved in the JEBAR also generates a small depth-dependent cross-slope component of the flow with magnitude and sign depending on the Coriolis parameter.

The JEBAR in the EGC in Fram Strait has been shown by our model to contribute very efficiently both to the current transport and to the cross-slope structure of the depth-integrated flow. Within the range of friction parameters allowed by the model, the bottom transport

induced by the JEBAR ranges between 3 and 27 Sv, that is, from a similar order to one order of magnitude larger than the relative geostrophic transport. When a 4 Sv bottom transport is assumed, the predicted cross-slope structure of the depth-integrated flow, especially the location of the maxima of the velocity and of the transport, roughly follows that of the JEBAR-induced flow. Finally, although the cross-slope structure of the alongslope flow at the surface is dominated by a large maximum of the surface-intensified relative-to-bottom flow, at a distance from the coast of about two-thirds of the slope width, the JEBAR-induced bottom velocity appears to be able to create, for sufficient predominance of the internal friction, a secondary maximum of the surface velocity closer to the shelf break.

The flow characteristics in the model depend on the relative strength of the bottom and of the internal friction. For instance, in our particular context where the relative-to-bottom flow is fixed, the bottom transport as well as the total current transport decrease as the relative amount of internal friction, and the proportion of the JEBAR flow entering the relative-to-bottom flow, increase. Simultaneously, an increase of the relative strength of the internal friction moves upslope the characteritic local features of the flow, such as the maxima of the alongslope velocity and transport.

Some features observed in the few existing current meter measurements over the Greenland slope in Fram Strait can be explained based on the friction regimes displayed in the model. In particular, the observations reveal (i) an upslope increase of the southward flow near the bottom, (ii) an offshore component of the near-bottom flow, and (iii) a clockwise turning of the horizontal velocity vector with depth. According to the model, these features suggest that both bottom and internal friction operate, but perhaps more important is the internal friction. The small amount of bottom friction necessary to maintain a weak flow in the vicinity of the coast is consistent with a realistic value of the drag coefficient.

By combining information from the MIZEX 84 experiment with the assumption of a transport equally distributed between the relative-to-bottom and the bottom component of the geostrophic flow, the total alongslope transport in the EGC at 78.4°N in summer 1984 has been postulated to be about 8 Sv. Although our value may appear somewhat arbitrary, it is surprisingly consistent with statistical mechanics estimates of the individual in- and outflows through Fram Strait corresponding to an ocean equilibrium with maximum entropy. The inviscid theory would support an outflow of about 5 Sv through Fram Strait [see, e.g., Eby and Holloway 1994, Eq. (2)]. On the other hand, our transport of 8 Sv is close to the estimate made by Aagaard and Greisman (1975) based on an Arctic Ocean mass budget that, in Fram Strait, neglects the deep exchange below 700 m and considers a zero net transport in the upper and intermediate layers. In our case, a nonnegligible part of the EGC transport occurs below 700 m, with more than 1 Sv carried out by the relative component (Fig. 3) and, based on our model geometry, about 1.5 Sv by the bottom component. Assuming that the other components of the Arctic Ocean mass budget proposed by Aagaard and Greisman would still be correct, this deep outflow in the EGC should be compensated by an additional inflow of at least 2 Sv to the Arctic Ocean. Such an inflow may take place over the Barents Sea (e.g., Loeng et al. 1993), a contribution entirely neglected by Aagaard and Greisman.

Acknowledgments. We would like to thank the editor and the two anonymous reviewers for their thoughtful criticisms and their very helpful suggestions. This work was part of the ESOP-2 project supported by the MAST III programme of the Comission of the European Communities (Contract MAS3-CT95-0015).

REFERENCES

Aagaard, K., 1970: Wind-driven transports in the Greenland and Norwegian seas. *Deep-Sea Res.,* **17,** 281–291.

——, and L. K. Coachman, 1968: The East Greenland Current north of Denmark Strait, 1. *Arctic,* **21,** 181–200.

——, and P. Greisman, 1975: Toward new mass and heat budgets for the Arctic Ocean. *J. Geophys. Res.,* **80,** 3821–3827.

——, J. H. Swift, and E. C. Carmack, 1985: Thermohaline circulation in the Arctic mediterranean seas. *J. Geophys. Res.,* **90,** 4833–4846.

Broecker, W. S., 1991: The great ocean conveyor. *Oceanography,* **42,** 79–89.

Budeus, G., and W. Schneider, 1995: On the hydrography of the Northeast Water Polynya. *J. Geophys. Res.,* **100,** 4287–4299.

Csanady, G. T., 1985: ''Pycnobathic'' currents over the upper continental slope. *J. Phys. Oceanogr.,* **15,** 306–315.

Eby, M., and G. Holloway, 1994: Sensitivity of a large-scale ocean model to a parameterization of topographic stress. *J. Phys. Oceanogr.,* **24,** 2577–2588.

Fahrbach, E., C. Heinze, R. Rohardt, and R. A. Woodgate, 1995: Moored current meter measurements in the East Greenland Current. *Extended Abstracts, Nordic Seas Symp. on the Results of the Greenland Sea Project (GSP) 1987–1993,* Hamburg, Germany, Arctic Ocean Science Board and Sonderforschungsbereich ''Processes Relevant to Climate,'' 57–60.

Foldvik, A., K. Aagaard, and T. Torresen, 1988: On the velocity field of the East-Greenland Current. *Deep-Sea Res.,* **35,** 1335–1354.

Greisman, P., 1976: Current measurements in the eastern Greenland Sea. Ph.D. dissertation, University of Washington, 145 pp. [Available from Department of Oceanography, University of Washington, Seattle, WA 98195.]

Hakkinen, S., and D. J. Cavalieri, 1989: A study of oceanic surface heat fluxes in the Greenland, Norwegian, and Barents Seas. *J. Geophys. Res.,* **94,** 6145–6157.

Hunkins, K., and J. A. Whitehead, 1992: Laboratory simulation of exchange through Fram Strait. *J. Geophys. Res.,* **97,** 11 299–11 321.

Huthnance, J. M., 1984: Slope currents and ''JEBAR.'' *J. Phys. Oceanogr.,* **14,** 795–810.

Jónsson, S., 1991: Seasonal and interannual variability of wind stress curl over the Nordic Seas. *J. Geophys. Res.,* **96,** 2649–2659.

Legutke, S., 1991: A numerical investigation of the circulation in the Greenland and Norwegian Seas. *J. Phys. Oceanogr.,* **21,** 118–148.

Loeng, H., V. Ozhgin, B. Adlandsvik, and H. Sagen, 1993: Current measurements in the northeastern Barents Sea. ICES C.M., 1993/

C:41, Hydrographic Committee, 22 pp. [Available from ICES, Palægade 2–4, DK-1261 Copenhagen K, Denmark.]

Manley, T. O., K. L. Hunkins, and R. D. Muench, 1987: Current regimes across the East Greenland Polar Front at 78°40' north latitude during summer 1984. *J. Geophys. Res.*, **92,** 6741–6753.

Maslowski, W., 1996: Numerical simulations of topographic Rossby waves along the East Greenland Front. *J. Geophys. Res.*, **101** (C4), 8775–8787.

Mertz, G., and D. G. Wright, 1992: Interpretations of the JEBAR term. *J. Phys. Oceanogr.*, **22,** 301–305.

Moritz, R., and R. Colony, 1988: Statistics of ice motion, Fram Strait to North Pole. *Proc. Seventh Int. Conf. on Offshore Mechanics and Arctic Engineering*, Vol. 4, New York, NY, American Society of Mechanical Engineers, 75–82.

Mosby, H., 1962: Water, mass and heat balance of the North Polar Sea and of the Norwegian Sea. *Geofys. Publ.*, **24**, 289–313.

Myers, P. G., A. F. Fanning, and A. J. Weaver, 1996: JEBAR, bottom pressure torque, and Gulf Stream separation. *J. Phys. Oceanogr.*, **26,** 671–683.

Paquette, R. G., R. Bourke, J. F. Newton, and W. Perdue, 1985: The East Greenland Polar Front in autumn. *J. Geophys. Res.*, **90,** 4866–4882.

Rudels, B., 1987: On the mass balance of the Polar Ocean with special emphasis on the Fram Strait. *Nor. Polarinst. Skr.*, **188,** 1–53.

Sakamoto, T., and T. Yamagata, 1996: Seasonal transport variations of the wind-driven ocean circulation in a two-layer planetary geostrophic model with a continental slope. *J. Mar. Res.*, **54,** 261–284.

Salmon, R., 1990: The thermocline as an ''internal boundary layers.'' *J. Mar. Res.*, **48,** 437–469.

——, 1994: Generalized two-layer models of ocean circulation. *J. Mar. Res.*, **52,** 865–908.

——, and R. Ford, 1995: A simple model of the ''joint effect of baroclinicity and relief'' on ocean circulation. *J. Mar. Res.*, **53,** 211–230.

Schlichtholz, P., and M.-N. Houssais, 1995: Modification of a variational method for reconstruction of hydrographical fields in Fram Strait. *Extended Abstracts, Nordic Seas Symp. on the Results of the Greenland Sea Project (GSP) 1987–1993*, Hamburg, Germany, Arctic Ocean Science Board and Sonderforschungsbereich "Processes Relevant to Climate," 177–180.

Schott, F., and H. Stommel, 1978: Beta spirals and the determination of the absolute velocities in different oceans. *Deep-Sea Res.*, **25,** 961–1010.

Slordal, L. H., and J. E. Weber, 1996: Adjustment to JEBAR forcing in a rotating ocean. *J. Phys. Oceanogr.*, **26,** 657–670.

Stigebrandt, A., 1981: A model for the thickness and salinity of the upper layer of the Arctic Ocean and the relationship between ice thickness and some external parameters. *J. Phys. Oceanogr.*, **11,** 1407–1422.

Strass, V. H., E. Fahrbach, U. Shauer, and L. Sellmann, 1993: Formation of Denmark Strait overflow water by mixing in the East Greenland Current. *J. Geophys. Res.*, **98,** 6907–6919.

Wadhams, P., A. E. Gill, and P. F. Linden, 1979: Transects by submarine of the East Greenland Polar Front. *Deep-Sea Res.*, **26A,** 1311–1327.